Journal of Materials Chemistry A

ROYAL SOCIETY OF CHEMISTRY

PAPER

View Article Online
View Journal | View Issue

Cite this: J. Mater. Chem. A, 2023, 11, 22922

Unveiling the structure and ion dynamics of amorphous $Na_{3-x}OH_xCl$ antiperovskite electrolytes by first-principles molecular dynamics†

Tan-Lien Pham,[a] Mohammed Guerboub,[b] Assil Bouzid,[c] Mauro Boero,[b] Carlo Massobrio,[b] Young-Han Shin *[a] and Guido Ori *[b]

Sodium oxyhalide and hydroxyhalide antiperovskites are promising solid-state electrolytes (SSEs) because of their low melting point and rapid synthesis and, as such, they are becoming competitive with respect to other systems. While the structure and the mechanism underlying the ion dynamics are increasingly well understood in crystalline antiperovskites, their amorphous counterpart lacks precise structural characterization, hampering any conclusive insight into their properties. In this work, we resort to first-principles molecular dynamics within the Car–Parrinello scheme to assess the structure and ion dynamics of amorphous $Na_{3-x}OH_xCl$ (with $x = 0$, 0.5, and 1) antiperovskites at a quantitative level. We obtain a detailed structural description of these amorphous systems, unveiling the mechanism inherent to the dynamics of Na ions, the role of H atoms, and the resulting ionic conductivity. Our results demonstrate that the structure of amorphous Na_3OCl significantly differs from its crystal phase, showing very limited intermediate-range order and a short-range order mainly driven by four-fold Na atoms. Our results reveal that there is no evidence of phase separation in the amorphous $Na_{3-x}OH_xCl$, unlike the previous conjectured model of glassy Li_3OCl. The amorphous structure of Na_3OCl features remarkable Na ion dynamics and ionic conductivity, rivaling that of defective crystalline phases and highlighting its potential as a promising solid-state electrolyte. In hydroxylated models, the presence of hydroxyl OH^- anions plays a crucial role in the mobility of Na ions. This is facilitated by the rapid rotation of O–H bonds and paddlewheel-type mechanisms, leading to enhanced ion mobility in the amorphous $Na_{3-x}OH_xCl$ systems. This work provides unprecedented physical and chemical insight into the interplay between the structure, bonding, and ion transport in amorphous sodium-rich oxyhalide and hydroxyhalide antiperovskites, paving the way to their practical realization in next-generation SSEs.

Received 6th March 2023
Accepted 26th September 2023

DOI: 10.1039/d3ta01373a

rsc.li/materials-a

1 Introduction

Over the past decade, low-melting-point Li- and Na-rich antiperovskite solid electrolytes (SEs) have been targeted worldwide as promising materials for solid-state batteries because of their structural flexibility, high ionic conductivity, wide electrochemical window, and stability.[1–5] In particular, sodium oxyhalide and hydroxyhalide antiperovskites hold the potential to be used in the SE domain due to their low melting point (T_m < 300 °C), affordable cost and low environmental impact of the constituent elements (Na, H, O, and Cl), and rapid synthesis.[6] By exploiting their versatile structure, expressed as X_3OA (X= Li^+ or Na^+; A = halides (Cl^-, Br^-, I^-) or other anions (BH_4^- and NO_2^-)), the properties, performance and ion dynamics mechanisms of antiperovskite SEs can be tailored through chemical doping, defect tuning, and structural manipulation, thereby providing an exploitable multifaceted chemistry.[1,7–15] By virtue of aliovalent doping or *via* mixed hydroxides, Li-rich antiperovskites have been shown to yield "superionic" ion conductivities, *i.e.* ~0.1 mS cm^{-1}.[6,16] Beyond the stoichiometric X_3OA crystalline systems, attention has been drawn to the use of cation- and anion-doped X_3OA as well as glassy (or amorphous) antiperovskite electrolytes.[7,17,18] Glassy Li_3OCl- and Na_3OCl-based antiperovskites have been originally exploited by the teams of Braga and Goodenough, showing a glass transition temperature in the range 390–450 K and a conductivity of the order of 10^{-2} S cm^{-1} at room temperature.[19–21] However, attempts at reproducing the original laboratory synthesis were not conclusive and, to date, the structure and ion conduction mechanism of glassy antiperovskite electrolytes remain unsolved issues.[1,17,22–24]

[a]Multiscale Materials Modeling Laboratory, Department of Physics, University of Ul-san, Ulsan 44610, Republic of Korea. E-mail: xxxx@aaa.bbb.ccc

[b]Université de Strasbourg, CNRS, Institut de Physique et Chimie des Matériaux de Strasbourg, UMR 7504, F-67034 Strasbourg, France. E-mail: guido.ori@ipcms.unistra.fr

[c]Institut de Recherche sur les Céramiques, UMR 7315 CNRS-Univesité de Limoges, Centre Européen de la Céramique, 12 Rue Atlantis, 87068 Limoges Cedex, France

† Electronic supplementary information (ESI) available. See DOI: https://doi.org/10.1039/d3ta01373a

The original work of Braga *et al.*[19] was later questioned by Hanghofer *et al.*,[22] who ascribed the high conductivity of Li^+ ions to the presence of impurities and the stability of the sample, and the formation of $LiCl{\cdot}H_2O$ to the presence of H_2O. The results of ref. 19 have been substantiated by *ab initio* and classical molecular dynamics (MD) simulations agreeing on the existence of a subnanoscale phase separation of Li_3OCl into Li_2O and LiCl phases together with an intermixed phase. The formation of such subnanoscale separation was considered to be the promoter of the high conductivity of Li ions as well as a non-negligible Cl ion mobility.[25] Choi *et al.* further characterized by *ab initio* MD the structural and electrochemical stability of amorphous Li_3OCl.[26]

Successful use of an electrolyte composite was recently reported by Tian *et al.*[27–29] In this application, amorphous Li_3OCl was used as a matrix embedding $Li_{6.75}La_3Zr_{1.75}Ta_{0.25}O_{12}$ garnet-type oxide particles exhibiting a high room temperature conductivity of 2.27×10^{-4} S cm^{-1} and an extremely wide electrochemical stability window up to 10 V. In this particular case, the added value promoted by the amorphous X_3OA phase was the ability to act as a binder and filling agent ensuring the formation of an integrated composite SE with a continuous widespread ionic conductive network. The key role of the amorphous phase was also assigned to the excellent affinity to the lithium metal, greatly decreasing the interfacial resistance between the anode and the electrolyte.[27–29]

A detailed understanding of the atomic structure is a key step to further capture the details of the transport mechanisms behind its conductivity performance. Recent reviews on the use of anti-perovskites for solid-state batteries underlined the limited nature of the available structural characterization and pointed out the severe need for a quantitative structural assessment to avoid any misinterpretation of the correlations between the structure and performances.[1,30,31] Overall, the structure and ion dynamics mechanisms are well known for crystalline X_3OA compounds. This is not the case for amorphous antiperovskites, especially in both hydrogen-free and hydroxylated phases (*e.g.*, oxyhalide X_3OA *vs.* hydroxyhalide $X_{3-x}OH_xA$).

In view of these considerations, this work relies on predictive atomic-scale modelling, as first-principles molecular dynamics (FPMD), to elucidate the structure and transport properties of amorphous H-free and hydroxylated $Na_{3-x}OH_xCl$ systems.[32] In terms of structural analysis, we provide a detailed study of both X-ray and neutron structure factors. If the X-ray probe is of high importance, neutron studies are particularly needed in the case of antiperovskite electrolyte investigation, being capable of detecting low-Z elements (or light elements, such as H and Li) that are out of reach of X-ray (synchrotron source) techniques.[1,2,17,33]

Our paper is organized as follows. Section 2 describes the methodologies and model systems employed within first-principles molecular dynamics. We give details on the production of the amorphous systems allowing for the calculation of static and dynamical properties. A specific subsection is devoted to a set of definitions for structural (disorder degree) and dynamical (ionic diffusion and conductivities) quantities targeted in this work for their potential applications in solid-state electrolytes. Results are presented in Section 3 and separated into two subsections, with the first one (3.1) devoted to structural properties and the second one (3.2) to dynamical properties. The analysis of the structural properties features, firstly, calculated properties in reciprocal and real space (3.1.1 and 3.1.2), namely the structure factors and the pair correlation functions. The following parts are devoted to the analysis of the coordination numbers (3.1.3) and the structural units (3.1.4), with special attention paid to the chemical nature of the various motifs and their variations with the composition. A final part is devoted to the assessment of the structural disorder degree of the studied models (3.1.5).

Subsection 3.2 is organized into three parts, describing respectively the different trends shown by the mean square displacements (3.2.1), a dynamical structural rearrangement involving the hydroxyl group (the "paddlewheel" effects, 3.2.2), and the behavior of the diffusion coefficients (3.2.3) leading to the assessment of the ionic conductivity (3.2.4). Concluding remarks are collected in Section 4.

2 Calculation methodology and models

2.1 Producing $Na_{3-x}OH_xCl$ amorphous models at 300 K

The Car–Parrinello (CP) method[34] was used to produce dynamical trajectories of the targeted $Na_{3-x}OH_xCl$ systems. The exchange–correlation functional selected is the generalized gradient approximation (GGA) proposed by Perdew, Burke and Ernzerhof (PBE).[35] The valence–core interaction was described by numerical norm-conserving Troullier–Martins (TM)[36] pseudopotentials for all elements (Na, O, H, and Cl). In the case of Na, semi-core states were included to ensure a good description of the energetics and electronic features dependent on its cationic nature. This amounts to electronic configurations He $2s^2$, $2p^6$, $3s^1$ for Na; He $2s^2$, $2p^4$ for O; $1s^1$ for H and Ne $3s^2$, $3p^5$ for Cl. Valence electrons are treated explicitly and represented on a plane-wave basis set with the sampling of the Brillouin zone restricted to the Γ point. A fictitious electron mass of 600 a.u. and a time step of 0.12 fs ensured optimal conservation of the constants of motion. FPMD simulations were performed in a canonical NVT ensemble with the ionic temperature controlled with a Nosé–Hoover[37–39] thermostat chain.[40] For the simulations performed at high temperature (>1000 K) we used a Blöchl–Parrinello electronic thermostat[41] with a target kinetic energy of 0.1 a.u. to control the fictitious motion of the electronic degrees of freedom. Our FPMD approach[34,42] has been extensively used and benchmarked in the last few decades and contributed to the improvement of our understanding of both the physical and chemical properties of chalcogenide and chalcohalide glasses,[43–45] hybrid[46,47] and porous[48] systems, and nanomaterials.[49–52]

The Na_3OCl glass model was generated by quenching from the melt. The initial configuration consisted of a Na_3OCl crystal cubic unit cell replicated $3 \times 3 \times 3$ times to obtain a 135 atom model (81 Na, 27 O, and 27 Cl) in a cubic simulation cell of side

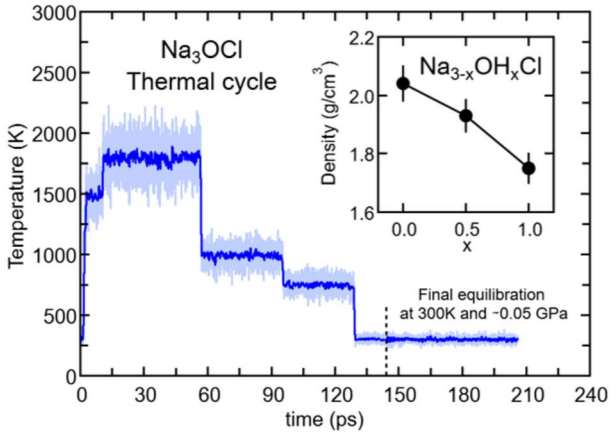

Fig. 1 (Color online) Temperatures along the thermal cycle for amorphous Na_3OCl: light blue line, instantaneous T values; blue line, T value sliding average with a window of 0.1 ps. The dashed vertical grey line sets the time at which the optimization of the volume at $T = 300$ K and 0 GPa was implemented. Inset: final density values optimized at $T = 300$ K for the three $Na_{3-x}OH_xCl$ models. Error bars are estimated with tests at different volumes performed on several final configurations (300 K) to obtain a final stress tensor close to 0 GPa (see Fig. S1 in the ESI†).

length 13.6148 Å.[53] The initial box was expanded by 15% with respect to crystal density in order to ease melting at a high temperature. A similar approach was followed for the case of glassy Li_3OCl.[25] Periodic boundary conditions were applied throughout. The model underwent a thermal cycle *via* canonical NVT simulations, according to the following protocol: 1.3 ps at $T = 300$ K, 1.2 ps at $T = 1200$ K, 3.1 ps at $T = 1500$ K, 46.5 ps at $T = 1800$ K, 38.6 ps at $T = 1000$ K, 33.7 ps at $T = 750$ K and 35 ps at $T = 300$ K (see Fig. 1). At the end of the cycle of $T = 300$ K, the density of the system was set to 2.04 g cm^{-3} (corresponding to a final volume expansion of +5% with respect to the crystal phase) in order to reduce the stress tensor to values very close to 0 GPa. Along the thermal cycle the energy cutoff for the plane wave expansion was $R_{Ec} = 80$ Ry. This value was increased at $T = 300$ K ($R_{Ec} = 160$ Ry) with a reduced time step of 0.072 fs to achieve the convergence of the stress tensor (see Fig. S1 in the ESI†). By using the final configuration of amorphous Na_3OCl at $T = 300$ K, we randomly replaced an appropriate number of Na atoms with H atoms to obtain $Na_{2.5}OH_{0.5}Cl$ and Na_2OHCl (corresponding to ~17% and ~33% of Na replaced, respectively). These systems underwent a thermal cycle *via* canonical NVT simulations with the following time schedule: 20 ps at $T = 1800$ K, 22 ps at $T = 1000$ K, 19 ps at $T = 750$ K, and 30 ps at $T = 300$ K. To obtain vanishing pressure at $T = 300$ K, the density of the system was set to 1.93 g cm^{-3} ($Na_{2.5}OH_{0.5}Cl$) and 1.75 g cm^{-3} (Na_2OHCl) (Fig. 1 inset). In what follows, the results on the atomic structure are presented as time-average values over the last 20 ps of the thermal cycles at $T = 300$ K. For all the simulations performed here, we used the developer version of the CPMD package.[54]

With respect to the quantification of the disorder degree of the different models, herein we report the main feature of the smooth overlap of the atomic positions (SOAP) descriptor employed. In the SOAP formalism, the density of the neighborhood surrounding the i-th atom is smoothed using descriptor functions that encode regions of atomic geometries with respect to atomic neighbor environments within a finite cutoff radius using a local expansion of a Gaussian smeared atomic density $\rho^{i,a}(\mathbf{r})$ with orthonormal functions based on spherical harmonics $Y_l^m(\hat{\mathbf{r}})$ and radial basis functions $R_n(\mathbf{r})$.[55,56] In this study, we computed the average summation $\mathbf{p}(\mathbf{r})$ vector for the Cl atoms,[57] being the only element present in equal amounts in all three models. The formula for computing the SOAP $\mathbf{p}(\mathbf{r})$ vector is given by:

$$\mathbf{p}^{i,aa'}_{nn'l}(\mathbf{r}) = \frac{1}{\sqrt{2l+1}} \sum_m \left(c^{i,a}_{nlm}\right)^* c^{i,a'}_{n'lm} \quad (1)$$

where $c^{i,a}_{nlm}$ is defined by:

$$c^{i,a}_{nlm}(\mathbf{r}) = \int R_n(r)^* Y_l^m(\hat{\mathbf{r}})^* \rho^{i,a}(\mathbf{r}) \mathrm{d}\mathbf{r} \quad (2)$$

and

$$\rho^{i,a}(\mathbf{r}) = \sum_j \delta_{aa_j} \exp\left[\frac{-|\mathbf{r}_i - \mathbf{r}_j|^2}{2\sigma_a^2}\right] f_{\mathrm{cut}}(\mathbf{r}_{ij})$$

where the sum is over neighbours j of element a that is within the cutoff and $f_{\mathrm{cut}}(\mathbf{r})$ is a cutoff function that smoothly goes to zero at $\mathbf{r}_{\mathrm{cut}}$. The hyperparameter σ_a has units of length and determines the regularity (smoothness) of the representation. The absolute value of the SOAP $\mathbf{p}(\mathbf{r})$ vector depends on the number of species, number of descriptors calculated, and cutoff radius, making it a valuable tool for analyzing specific systems. For this study, a = Cl and a' is one of those elements Cl, Na, O, or H with a cutoff radius of 5.5 Å that was chosen to encompass the next-nearest neighbor environments. $\sigma_a = 1$, $n_{\max} = 10$ and $l_{\max} = 8$. The final number of descriptors computed correspond to 4185 for Na_3OCl and 7380 for the two hydroxylated models.

2.2 Dynamical simulations at finite temperatures

FPMD simulations allow the assessment of the transport properties of mobile ions in amorphous materials.[58,59] In this work, the ion dynamics and transport properties were studied at different temperatures, specifically $T = 300$ K, 450 K, 600 K, 800 K, 1000 K, and 1200 K (Na_3OCl only). The three systems were equilibrated in a NVT canonical ensemble for a total simulation time of ~50 ps. Trajectories were collected every 20 steps (1.45 fs). The mean square displacements (MSDs) of all ions were computed according to

$$\langle r^2(t) \rangle = \left\langle \sum_{i=1}^{N} |r_i(t) - r_i(0)|^2 \right\rangle = \left\langle \sum_i (\Delta \mathbf{R}_i(t))^2 \right\rangle \quad (3)$$

where N is the number of the atoms of interest and $\langle \sum_i (\Delta \mathbf{R}_i(t))^2 \rangle$ is the MSD averaged on all realizations of eqn (3) for a given value of time t. It should be noted that in its standard definition, the mean square displacement is normalized to the number of particles, say N, so as to appear as an intensive property resulting from an average over the whole system.

However, for the sake of convenience, we prefer to take advantage of a definition of the MSD taking the form of eqn (3). To assess the so-called tracer diffusive D^* behavior of the ions, the MSD is analysed in log–log plots *via* the slopes $\beta(t)$ as a function of time,

$$\beta(t) = \frac{d\log\left\langle \sum_i (\Delta \mathbf{R}_i(t))^2 \right\rangle}{d\log\ t} \quad (4)$$

At very short t, a value of $\beta(t)$ equal to two is expected, corresponding to a free, ideally ballistic motion of the ions, while at very long times, $\beta(t)$ should reach a value equal to one, corresponding to a real diffusive regime, with the MSD growing linearly with time. We would like to stress here that this analysis is crucial to determine the effective achievement of diffusive behavior and identify the portion of the MSD plot that should be used to extract diffusion coefficients. This is particularly important in the case of disordered materials such as glasses,[60] ionic liquids,[61] and molten salts.[62] In the present work, the lower and upper bounds of the real diffusive regime were defined within the interval delimited by (lower boundary) the t at which $\beta(t)$ reaches a value of one up to (upper boundary) the value of t corresponding to a length of trajectory 15% shorter than the total one.[63] For the systems that reach the diffusive regime at a given temperature, the ion diffusion coefficients (*e.g.* tracer diffusivity) were calculated by using the Einstein relation given by:[64,65]

$$D^* = \lim_{t\to\infty} \frac{1}{N2d} \frac{\partial\langle r^2(t)\rangle}{\partial t} \simeq \frac{\sum_i \langle \Delta \mathbf{R}_i^2\rangle}{N2dt} \quad (5)$$

where d is the dimensionality factor ($d = 3$ for three dimensional systems) and we have eliminated the explicit dependence on time in eqn (5) as a result of the infinite t limit. When the diffusive regime is reached, the Arrhenius equation can be used to calculate the activation energy E_a barrier for diffusion (conductivity) by fitting the data of $\log D^*$ ($\log\sigma^*$) *vs.* $1/T$ as:

$$D^* = D_0 \exp\left(-\frac{\Delta E_a}{kT}\right) \quad (6)$$

From the tracer diffusivity D^*, the idealized ionic conductivity can be calculated based on the Nernst–Einstein relation:

$$\sigma^* = D^*\ \frac{Nq^2}{VkT} = \frac{q^2}{2dVkT} \sum_i \langle \Delta \mathbf{R}_i^2\rangle \quad (7)$$

where V is the total volume of the model system, q is the charge of mobile-ion species, T is the temperature, and k is the Boltzmann constant. A more accurate estimation of the relevant conductivity is instead given by the Einstein formulation of the net charge migration as:

$$\sigma_{ion} = D_\sigma\ \frac{Nq^2}{VkT} = \frac{q^2}{2dVkT} \left\langle \left(\sum_i \Delta \mathbf{R}_i\right)^2 \right\rangle \quad (8)$$

The charge-diffusion coefficient D_σ, which refers to the displacement of the center of mass of all the diffusing ions and is used here to consider possible correlation effects, is defined as:

$$D_\sigma = \frac{\left\langle \left(\sum_i \Delta \mathbf{R}_i\right)^2 \right\rangle}{2dNt} = \frac{\sum_i \langle \Delta \mathbf{R}_i^2\rangle}{2dNt} + \frac{\sum_i \sum_{ii\neq i} \langle \Delta \mathbf{R}_i \Delta \mathbf{R}_{ii}\rangle}{2dNt} \quad (9)$$

where d is the dimension of the lattice where diffusion takes place and N refers to the number of diffusing ions.[66–69] The numerator on the left-hand side was split into a self-diffusion part and a distinct-ion part, with the latter accounting for correlations between the movements of distinct ions of the same type (*i.e.* Na ions).

The Haven ratio is a measure of the degree by which the trajectories of different atoms are correlated to each other.[66,70] For single ion conductors, it is

$$H_R^\sigma = \frac{D^*}{D_\sigma} \quad (10)$$

becoming equal to one in the absence of any correlation between different diffusing atoms. This is asymptotically approached in the dilute limit, where diffusing atoms rarely encounter each other during their motion through a crystal. If distinct ions move preferentially in the same direction (positive correlation), then $H_R > 0$ and $H_R < 1$, which is usually observed for single-ion conductors.[69,71–73] At non-dilute concentrations, as in the majority of solid electrolytes, positive correlations between different diffusing ions become particularly relevant, resulting in $H_R < 1$, whereas negative correlations between different diffusing ions (distinct ions move preferentially in the opposite directions) give $H_R > 1$. To consider all types of ion correlations (positive and negative) involved in the system, namely cation–cation correlations (σ_{++}^{dist}), anion–anion correlations (σ_{--}^{dist}) and cation–anion correlations (σ_{+-}^{dist}) contributing to the Haven ratio, the following equation is used:

$$H_R^{tot} = \frac{\sigma^{*tot}}{\sigma_{ion}^{tot}} = \frac{\sigma_+^{self} + \sigma_-^{self}}{\sigma_{ion}^{tot}} = \frac{\sigma_{Na}^{self} + \sigma_O^{self} + \sigma_{Cl}^{self}}{\sigma_{Na,O,Cl}^{self} + \sigma_{NaNa,OO,ClCl}^{dist} + 2\sigma_{NaCl,NaO,ClO}^{dist}} \quad (11)$$

where

$$\sigma_{ion}^{tot} = \frac{q^2}{2dVkT} \left\langle \left(\sum_i^N z_i \Delta \mathbf{R}_i\right)^2 \right\rangle \quad (12)$$

$$\sigma_A^{self} = \frac{q^2 z_A^2}{2dVkT} \sum_i \langle \Delta \mathbf{R}_i^2\rangle \quad (13)$$

$$\sigma_{AA}^{dist} = \frac{q^2 z_A^2}{2dVkT} \sum_i \sum_{ii\neq i} \langle \Delta \mathbf{R}_i \Delta \mathbf{R}_{ii}\rangle \quad (14)$$

$$\sigma_{AB}^{dist} = \frac{q^2 z_A z_B}{2dVkT} \left(\sum_i \Delta \mathbf{R}_i \sum_j \Delta \mathbf{R}_j\right) \quad (15)$$

N is the total number of ions in the electrolyte, and z_i is the charge number of ion i.[61] The sum in eqn (11) can be re-expressed as shown in eqn (12)–(15). H_R^{σ} is computed by considering correlation effects only promoted by Na ions, whereas with H_R^{tot} the contribution of possible correlation effects due to O and Cl ions is also taken into account. These equations are an alternative to the methods based on quantifying collective correlated effects by integration of the ion velocity autocorrelation functions.[74–76]

3 Results and discussion

3.1 Structural properties

3.1.1 Total X-ray and neutron structure factors. The total X-ray and neutron structure factors ($S_T^X(k)$ and $S_T^N(k)$, respectively) can be directly calculated on the equilibrium trajectory in the reciprocal space.[77,78] Alternatively, $S_T^X(k)$ can be obtained by Fourier transform (FFT) of the real space total pair correlation function $g_{tot}(r)$. We underline that the calculation of $S_T(k)$ directly in the k-space is, generally, to be preferred over the Fourier transform of the real-space pair distribution functions, since the former approach avoids the effects of the finite range of integration. However, the FFT procedure is currently adopted in the literature to smooth out the noise affecting the structure factors computed directly in reciprocal space, especially in the case of glassy configurations at room temperature. In the present work, we employed the FFT method and the calculated $S_T^X(k)$ and $S_T^N(k)$ are shown in Fig. 2.

In the following, we analyze X-ray and neutron FFT $S_T(k)$ in terms of peak positions and intensities comparing the three $Na_{3-x}OH_xCl$ systems. We remark that $S_T^X(k)$ of Na_3OCl features a first peak at about $k \sim 2.5$ Å^{-1} with a shoulder at $k \sim 2.0$ Å^{-1} and a second peak at $k \sim 3.5$ Å^{-1}. These first two peaks are followed by much broader maxima and minima and rapidly damped oscillations up to $k \sim 8.0$ Å^{-1}. $Na_{2.5}OH_{0.5}Cl$ and Na_2OHCl $S_T^X(k)$ have very similar profiles and minor differences with respect to pristine Na_3OCl. In contrast, while the X-ray structure factor $S_T^X(k)$ exhibits similarities across all three cases, the neutron structure factor $S_T^N(k)$ displays significant distinctions, indicating that it may be a better diagnostic tool for discerning models containing varying amounts of hydrogen. Higher intensities are found in $S_T^N(k)$ for Na_3OCl. By increasing x, maxima and minima are reduced and different profiles appear in between $k \sim 2$ Å^{-1} and $k \sim 4$ Å^{-1} to signify a lower degree of structural organization. The relatively small peak at about $k \sim 1$ Å^{-1} reveals that the intermediate range order is very limited in these amorphous systems. Overall, Fig. 2 shows modifications taking place within the networks affecting an ordered structural sequence made of distinct shells of neighbors.

3.1.2 Total and partial pair-correlation functions. The total and partial pair correlation functions for the $Na_{3-x}OH_xCl$ ($x = 0$, $x = 0.5$, and $x = 1$) systems are shown in Fig. 3 and 4, respectively. In terms of total pair correlation functions, the H-free Na_3OCl one shows a first narrow peak centered at ~2.28 Å (with a full width at half maximum (FWHM) of 0.28 Å) and a broader second peak at a lower intensity at ~2.77 Å (FWHM of 0.47 Å). These two peaks are present also in the hydroxylated systems, although with a lower ratio between the intensities for $Na_{2.5}OH_{0.5}Cl$, whereas similar values are observed in Na_2OHCl.

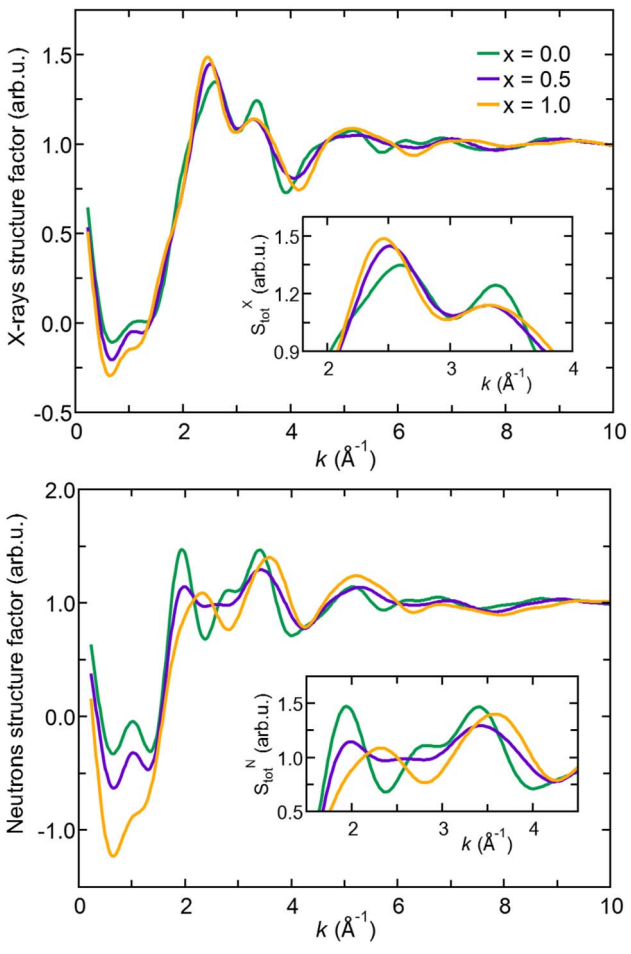

Fig. 2 (Color online) Total X-ray (top) and neutron (bottom) structure factors for amorphous $Na_{3-x}OH_xCl$ ($x = 0$, $x = 0.5$, and $x = 1$) obtained through Fourier transform of the total pair correlation functions at $T =$ 300 K. Insets: zoomed-in view of the 1.8–4.0 Å^{-1} and 1.5–4.5 Å^{-1} ranges, respectively.

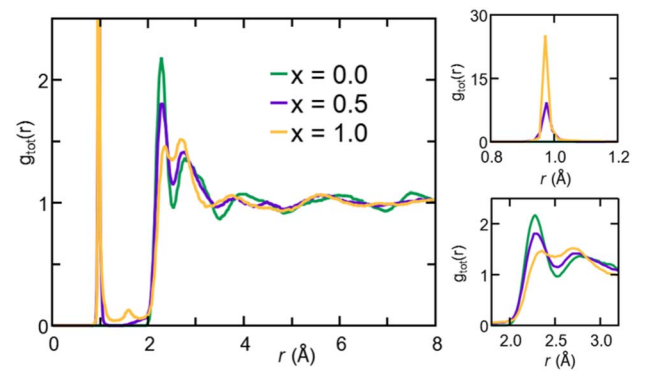

Fig. 3 (Color online) Left: Total pair correlation functions for amorphous $Na_{3-x}OH_xCl$ ($x = 0$, $x = 0.5$, and $x = 1$) obtained at $T = 300$ K. Right: Zoomed-in view of the 0.8–1.2 (top) and 1.8–3.2 (bottom) ranges.

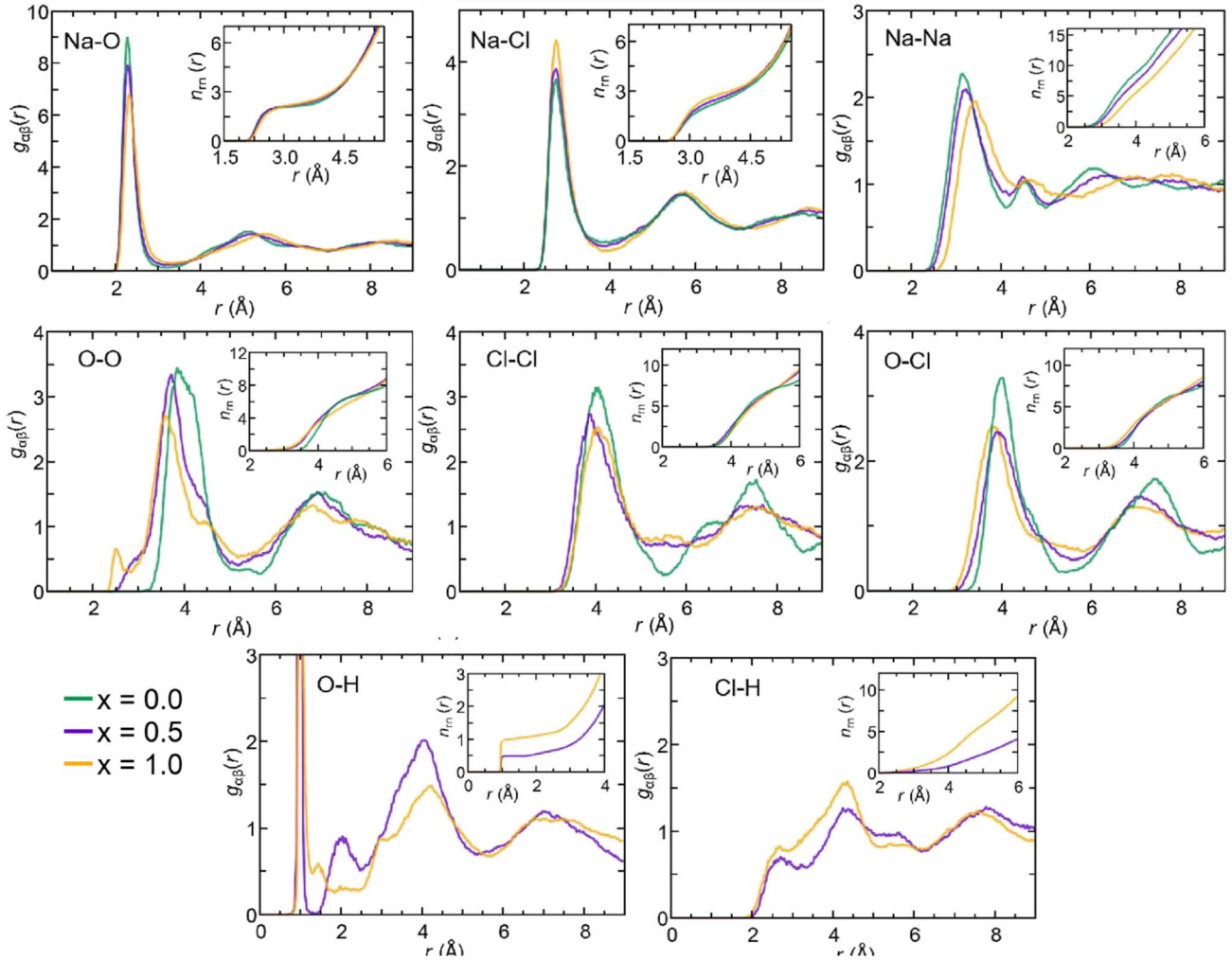

Fig. 4 (Color online) Partial pair correlation functions $g_{\alpha\beta}(r)$ for amorphous $Na_{3-x}OH_xCl$ ($x = 0$, $x = 0.5$, and $x = 1$) at $T = 300$ K relative to the pairs Na–O, Na–Cl, Na–Na, O–O, Cl–Cl, O–Cl, O–H, and Cl–H. The running integrals over the interatomic distance are shown.

As expected, the presence of H leads to a very sharp peak at about ~0.98 Å, with a FWHM of 0.02 Å. In addition, there is a very small maximum in Na_2OHCl at ~1.5 Å. Analyzing the partial pair correlation functions $g_{\alpha\beta}(r)$ (Fig. 4) allows us to trace back the role of each individual pair contribution with respect to the total one. In Table 1 we report the nearest-neighbor distances r_{ij} identified by the position of the first maximum of $g_{\alpha\beta}(r)$ for the three $Na_{3-x}OH_xCl$ systems. For comparison, we also report the nearest-neighbor distances found in synthesized pure crystalline Na_3OCl.[15,79] The first peak of $g_{tot}(r)$ for amorphous Na_3OCl can be ascribed entirely to the Na–O pair (~2.28 Å), whereas the second peak is mainly attributed to the Na–Cl pair (~2.75 Å) and only partially to Na–O and Na–Na (~3.14 Å) $g_{\alpha\beta}(r)$ contributions. The first peak of $g_{NaNa}(r)$ is responsible for the shoulder occurring after the second peak (~2.8–3.1 Å) found in the total pair correlation function. Analyzing the peak positions of $g_{NaO}(r)$ for amorphous Na_3OCl, the Na–O bond distance is found slightly larger than the typical ionic bond reported for crystalline Na_3OCl (~2.25 Å), whereas the Na–Cl ionic bond distance is shorter than that of the crystalline one (~3.18 Å). The partial pair correlation functions $g_{NaO}(r)$, $g_{NaCl}(r)$ and $g_{NaNa}(r)$ of the two hydroxylated systems are quite similar to those of Na_3OCl. However, the intensities of the first peaks in $g_{NaO}(r)$ and $g_{NaNa}(r)$ are reduced in accordance with the lower content of Na atoms (in favor of H atoms), whereas the corresponding intensity in $g_{NaCl}(r)$ is increased. Replacing some of the Na atoms with H atoms causes an elongation of the Na–O distance in Na_2OHCl (~2.32 Å for ~33% of Na atoms replaced), while no effect is found on the Na–O distance for $Na_{2.5}OH_{0.5}Cl$ (~2.27 Å for ~17% of Na atoms replaced). In contrast, Na–Cl bond distances found in $Na_{2.5}OH_{0.5}Cl$ and Na_2OHCl are the same as those in Na_3OCl (~2.75 Å). $g_{NaNa}(r)$ shows a slight increase of the Na–Na nearest-neighbour interatomic distances with increasing H content (up to ~3.34 Å when ~33% of Na is substituted). The two hydroxylated systems are affected by a greater degree of disorder in comparison with Na_3OCl as confirmed by a less pronounced minimum separating the peaks in $g_{NaNa}(r)$.

The $g_{OH}(r)$ partial pair correlation functions of $Na_{2.5}OH_{0.5}Cl$ and Na_2OHCl show that all H atoms are bonded to O atoms, forming OH hydroxyl groups with a typical O–H bond distance

Table 1 Upper part: nearest-neighbour interatomic distances r_{ij} (in Å) identified by the position of the first maximum of the pair correlation functions $g_{ij}(r)$. We also give the first peak full width at half maximum (FWHM). For comparison, we report the values of the crystalline Na_3OCl phase obtained by experiments.[53,79] Lower part: total and pair coordination numbers as defined by taking different cutoff radii for the definition of a total or a "cation–anion" shell of interactions (see Section 3.1.3). Values in parentheses correspond to the statistical uncertainty on the last reported digits

	Exp.[53,79]	FPMD, this work		
	Crystal	Na_3OCl	$Na_{2.5}OH_{0.5}Cl$	Na_2OHCl
r_{NaO}	2.25	2.28(2)	2.27(2)	2.32(2)
FWHM		0.28	0.31	0.33
r_{NaCl}	3.18	2.75(2)	2.75(3)	2.74(4)
FWHM		0.47	0.46	0.52
r_{NaNa}	3.18	3.14(3)	3.22(4)	3.34(4)
FWHM		0.92	1.01	1.02
r_{OO}	4.50	3.85(1)	3.72(4)	3.61(4)
FWHM		0.86	0.77	0.72
r_{OCl}	3.89	4.00(4)	3.91(2)	3.78(4)
FWHM		0.79	1.00	0.93
r_{ClCl}	4.50	4.06(3)	3.87(3)	4.05(3)
FWHM		0.82	1.04	1.01
r_{OH}	—	—	0.98(2)	0.97(2)
FWHM	—	—	0.02	0.02
n^t_{Na}	14	8.01(3)	7.26(2)	6.04(2)
n^p_{Na}	6	4.0(1)	4.30(1)	4.58(2)
n^t_O	6	6.30 (2)	6.44(2)	6.09(4)
n^p_{Na}	6	6.29 (3)	5.94(2)	5.40(2)
n^t_{Cl}	12	5.73(3)	5.45(2)	4.93(3)
n^p_{Cl}	12	5.72(1)	5.37(1)	4.78(3)
n^t_H	—	—	1.00(2)	1.02(3)

equal to ~0.98 Å. This observation is further supported by the analysis of $g_{ClH}(r)$, for which the Cl–H interatomic distance lies at values higher than ~2.0 Å for both the hydroxylated phases, much larger than the typical Cl–H bond distance, *i.e.* ~1.3 Å. For what concerns $g_{OH}(r)$, a few differences can be pointed out between the two hydroxylated phases. In $Na_{2.5}OH_{0.5}Cl$, a second peak exists at about ~2.0 Å, which reflects the presence of a H-bonding network promoted between neighboring hydroxyl groups or free oxygen atoms in the form of OH···OH and OH···O interactions, respectively. In Na_2OHCl, such a peak is minimally visible but a small peak at a shorter distance (~1.5 Å) is discernible. This latter peak is the one that generally identifies H atoms (or protons) hopping between neighboring hydroxyl groups and giving rise to stable or metastable water molecules.[80–85] In terms of anion–anion pair correlation functions, all three $g_{OO}(r)$, $g_{ClCl}(r)$ and $g_{OCl}(r)$ are characterized by a first main peak centered at around ~3.7–4.0 Å. There are interesting differences to be pointed out when comparing $g_{OO}(r)$ for the three $Na_{3-x}OH_xCl$ models. In particular, Na_3OCl exhibits a relatively broad first peak at ~3.85 Å (FWHM of ~0.86 Å), whereas the two hydroxylated models feature intense peaks at ~3.72 Å and ~3.61 Å (FWHM of ~0.77 Å and ~0.72 Å, respectively), followed by a shoulder centered at about ~4.5 Å. Also, a small peak at ~2.5 Å for $Na_{2.5}OH_{0.5}Cl$ and a shoulder at about ~2.9 Å for $Na_{3-x}OH_xCl$ are worth noticing, while in the case of Na_3OCl $g_{OO}(r)$ goes to zero for distances <3.2 Å. In terms of $g_{ClCl}(r)$ and $g_{OCl}(r)$, the three models show very similar profiles, although the intensity of the main peak of the two hydroxylated systems is smaller for a higher degree of disorder with respect to Na_3OCl.

3.1.3 Total and partial coordination numbers. More insights into the $Na_{3-x}OH_xCl$ networks can be obtained by looking at the total and partial coordination numbers (n_i and n_{ij}, respectively), obtained by relying on the pair correlation functions. More precisely, n_{ij} is obtained by integrating the first peak of $g_{ij}(r)$ up to a given cutoff distance corresponding to the position of the first minimum. The total Na, O, Cl, and H coordination numbers are then obtained as follows: $n_{Na} = n_{NaO} + n_{NaCl} + n_{NaNa} + n_{NaH}$, $n_O = n_{ONa} + n_{OH} + n_{OCl} + n_{OO}$, $n_{Cl} = n_{ClNa} + n_{ClH} + n_{OCl} + n_{ClCl}$ and $n_H = n_{HO} + n_{HCl} + n_{HNa} + n_{HH}$. When the first peak of the corresponding $g_{ij}(r)$ is followed by a clear minimum well separated from a second maximum, n_{ij} does not suffer from any ambiguities for its definition, since the running coordination number exhibits a clear plateau (see the behavior in the case of Na–O interactions, inset of Fig. 4). In the opposite case, the determination of n_{ij} is less clearcut (see the Na–Na case in the inset of Fig. 4) and n_{ij} is much more sensitive to the choice of the cutoff. For these reasons, in addition to the individual pair cutoffs taken as the minima after the first peak of $g_{ij}(r)$, we adopted a second cutoff (a "total" one) defined by the minimum after the second peak of $g_{tot}(r)$. The value found (3.3 Å) is determined as the average between the three amorphous models and it allows us to consider within the first coordination shell of Na atoms all the counter-ions (O and Cl) and a number of neighboring Na atoms. With this procedure, we can compare the coordination numbers of amorphous $Na_{3-x}OH_xCl$ models to those of the crystalline phase of Na_3OCl. We remind that crystalline Na_3OCl (cubic phase, stable at $T = 300$ K[15,53,79]) is characterized by Na atoms coordinated by six counter-ions (two oxygen and four chlorine atoms) within the nearest-neighbor shell, and O atoms are coordinated by six Na atoms and Cl atoms are coordinated by twelve Na atoms. Within the cutoff employed above (3.3 Å) each Na atom has also eight neighboring Na atoms, leading to a "total" Na coordination of 14.[53,79] Therefore, the local environment of Na in crystalline Na_3OC can be thought of as made up of a total of 14 neighboring atoms, with neighboring Na interacting through O atoms *via* Na–O–Na linkages (see Fig. 5a). On the basis of these considerations, we performed the analysis of the coordination numbers n_{ij} of amorphous $Na_{3-x}OH_xCl$ systems by considering the "partial" coordination number n^p_{ij} (definition 1) well adapted to describe the so-called "cation–anion" (*i.e.* counter-ions) interactions and the "total" coordination number n^t_{ij} (definition 2) that is most appropriate to describe the whole set of Na neighbors. The same distinction has been introduced to obtain the distribution of the structural coordination units characterizing the environment of each atom. For a given number of neighbors l and a given atomic species, one can extract from each configuration the chemical nature of the neighbors, providing a detailed description of the network organization. It is important to underline that a coordination number gives an average behavior stemming from all neighbors with no insight into the detailed

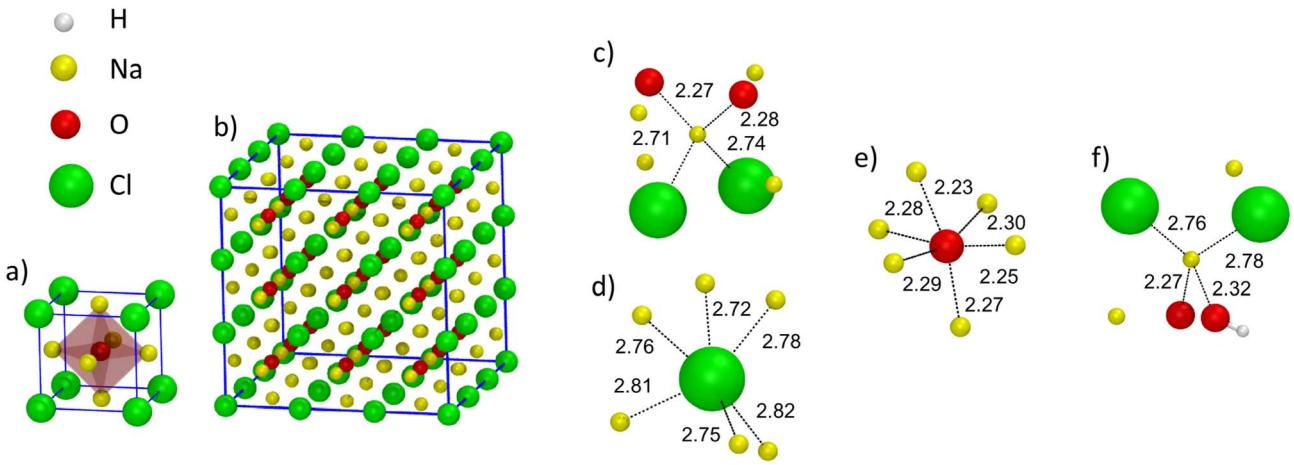

Fig. 5 (Color online) (a) Representation of the unit cell of crystalline Na_3OCl. The red polyhedra identify the octahedron O site. (b) Crystalline supercell of 135 atoms (unit cell replicated 3 × 3 × 3). (c–e) Coordination units for Na, O, and Cl found in amorphous Na_3OCl at $T = 300$ K: a fourfold Na atom (O_2Cl_2) (c), a sixfold Cl atom (d), and a sixfold O atom (e). (f) A Na atom found in amorphous $Na_{2.5}OH_{0.5}Cl$ coordinated by at least an O atom as a hydroxyl group. Counter-ion interatomic bonds are identified by a dashed line with the corresponding values. We show the atoms within a radial cutoff of 3.3 Å. Color legend: Na, yellow; O, red; Cl, green; H, white.

chemical nature of bonding, while the information provided by the coordination structural units shows how each atomic species organizes itself when connecting to atoms of the same or of a different kind. To help understanding these definitions, Fig. 5 contains snapshots of the local coordinations of the Na, O, and Cl atoms found in crystalline Na_3OCl as well as typical structural units in amorphous $Na_{3-x}OH_xCl$ systems issued from our calculations. Also, the insets of Fig. 4 show the running integrals of the individual partial correlation function $g_{ij}(r)$ from which we extracted the coordination numbers n_{ij}^t and n_{ij}^p given in Table 1. Focusing on the structural units, Fig. 6 provides their distribution in terms of the number l neighbors for Na, on the basis of definition 2. In terms of the total number of neighbours of Na atoms (within 3.3 Å), we observe that amorphous Na_3OCl exhibits a markedly distinct behavior when compared to its crystalline counterpart. Specifically, the unit distribution for Na atoms is remarkably wide (from 4 to 11) and centered at $l = 8.0$, with the number of neighboring counter-ions decreasing from six to four, and the number of Na neighbors halved from eight to four. The partial replacement of Na with H atoms induces a shift of the l unit distribution surrounding Na atoms to lower values, centered at ~7.3 and ~6.0 for $Na_{2.5}OH_{0.5}Cl$ and Na_2OHCl, respectively. By using definition 1, the distributions of structural units for Na, O, and Cl that account for what we termed counter-ion interactions are reported in Table 2, together with the breakdown of the chemical composition of each structural unit for a given l.

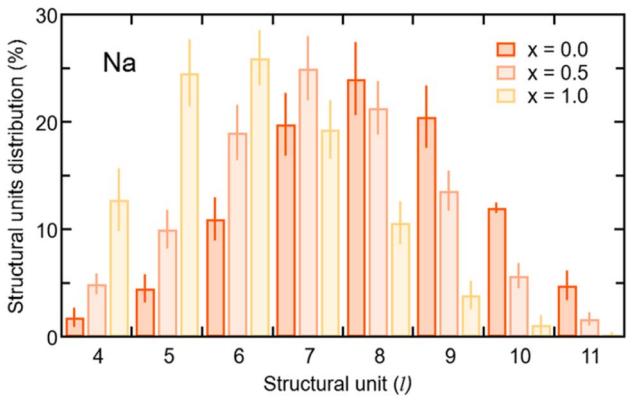

Fig. 6 Distributions of the structural units for Na of amorphous $Na_{3-x}OH_xCl$ ($x = 0$, $x = 0.5$, and $x = 1$) as a function of the number of neighbors in each unit (l). Values obtained by using the definition of "total" coordination n_{ij}^t, given in Section 3.1.3.

3.1.4 Chemical identification of the structural units for the three compositions. In the case of Na_3OCl, the coordination units given in Table 2 are indicative of a first coordination shell for Na essentially fourfold (~70.0%) in terms of cations–anions (*i.e.* counterions) according to definition 1 (see Section 3.1.3). The decomposition in terms of chemical species gives in decreasing order of importance the following units: O_2Cl_2 (~36.6%), O_3Cl_1 (~18.1%), O_1Cl_3 (~9.9%) and O_4 (~3.7%). Threefold and fivefold units correspond to ~14.6% and ~13.8%, respectively, with a larger presence of two or one oxygen atom (O_2Cl_1 ~10.4%, O_2Cl_3 ~5.4% and O_1Cl_4 ~4.4%). Our results demonstrate that the structure of amorphous Na_3OCl is significantly different from the molecular dynamics model conjectured for glassy Li_3OCl, based on nanophase segregation of regions rich in Li_2O and LiCl.[25] Indeed, by looking at Na atoms fourfold or even fivefold coordinated, in amorphous Na_3OCl only ~7.3% of them are exclusively coordinated to O atoms (O_3 and O_4) and ~1.5% are exclusively coordinated to Cl atoms (Cl_5). The value of n_O^t in amorphous Na_3OCl is about ~6.3 (Table 1), close to the one in crystalline Na_3OCl.[15,53,79] We find ~69.1% of O atoms coordinated by six Na atoms and ~27.6% by seven Na atoms (Table 2). For Cl, n_{Cl}^t is equal to ~5.7, almost half of that found in the crystalline phase (12). Several structural units connected to Cl are noticeable in Table 2. In fact, ~39.8% of Cl atoms are coordinated by six,

Table 2 Distribution of the individual cation–anion $n_\alpha(l)$ structural units, where an atom of species α (Na, Cl or O) is l-fold coordinated to a counter ion computed for glassy Na_3OCl (see definition 1, section "total and partial coordination numbers"). In bold are reported the total percentages determined for each l-fold coordination. These quantities have been calculated including neighbours separated by a cutoff corresponding to the first minimum in $g_{\alpha\beta}(r)$. For the present work, the individual pair cutoffs used are 3.30, 3.94, 4.10, 5.06, 5.51, and 5.39 Å for, respectively, the Na–O, Na–Cl, Na–Na, O–O, Cl–Cl and O–Cl distances. A total cutoff of 3.30 Å was defined from the total $g(r)$. Error bars are given in parentheses

		Proportions $\bar{n}_\alpha(l)$ (%)		
		$x = 0$	$x = 0.5$	$x = 1$
Na				
$l = 3$		**14.6**(1.9)	**8.4**(1.0)	**3.5**(1.0)
	O_2Cl_1	10.4	4.4	1.3
	O_3	3.6	2.5	0.6
$l = 4$		**70.0**(2.9)	**56.9**(2.2)	**43.8**(2.1)
	O_2Cl_2	36.6	23.8	13.1
	O_3Cl_1	18.1	13.9	14.5
	O_1Cl_3	9.9	11.8	11.0
	O_4	3.7	5.7	2.6
$l = 5$		**13.8**(1.5)	**30.4**(1.6)	**43.7**(2.3)
	O_2Cl_3	5.4	9.7	10.7
	O_1Cl_4	4.4	6.7	11.6
	O_3Cl_2	0.4	7.1	13.2
	Cl_5	1.5	2.5	1.5
$l = 6$		**3.3**(0.5)	**5.5**(0.7)	**11.1**(1.2)
	O_4Cl_2	—	0.3	2.3
	O_3Cl_3	—	1.3	2.3
	O_2Cl_4	0.5	1.0	1.8
	O_1Cl_5	0.2	1.1	1.7
O				
$l = 4$		—	<0.5	**8.6**(1.8)
	Na_2H_2	—	—	2.0
	Na_3H_1	—	0.4	6.6
$l = 5$		**2.1**(2.0)	**20.8**(3.9)	**44.4**(6.6)
	Na_3H_2	—	—	5.7
	Na_4H_1	—	16.5	38.6
	Na_5	1.9	4.3	0.1
$l = 6$		**69.1**(6.6)	**63.6**(4.9)	**44.7**(6.9)
	Na_5H_1	—	24.9	36.0
	Na_6	69.1	38.6	7.3
$l = 7$		**27.6**(6.1)	**15.0**(3.8)	**2.1**(1.9)
	Na_6H_1	—	6.1	2.0
	Na_7	27.6	8.9	—
Cl				
$l = 3$	Na_3H_0	—	**1.2**(1.0)	**4.8**(3.8)
$l = 4$	Na_4H_0	**8.2**(4.6)	**14.2**(8.7)	**31.5**(7.3)
$l = 5$	Na_5H_0	**31.6**(8.0)	**40.0**(8.6)	**45.4**(7.4)
$l = 6$	Na_6H_0	**39.8**(9.0)	**36.4**(7.7)	**16.9**(6.1)
$l = 7$	Na_7H_0	**17.1**(6.4)	**7.7**(4.4)	—
$l = 8$	Na_8H_0	**2.4**(1.9)	—	—

~31.6% by five, ~17.1% by seven and ~8.2% by four Na atoms. Having established the main features of the structural units in Na_3OCl, we can turn to the analogous description for the case of the hydroxylated amorphous materials. In $Na_{3-x}OH_xCl$ we observe a decrease of n^t_{Na} (from ~8.0 to ~6.0) from the value in Na_3OCl. However, n^p_{Na} does the opposite (from ~4.0 to ~4.6). The decrease in n^t_{Na} is due to the partial substitution of Na by H, with all the H atoms found coordinated to O atoms, forming in majority hydroxyl OH groups (n^t_H ~1.0). This is confirmed by the visual inspection of the snapshots relative to $Na_{2.5}OH_{0.5}Cl$ (Fig. 4e), where H is bonded to O atoms in the form of a hydroxyl group (O–H bonding distance ~0.98 Å), with no H–Na bond formation.

In terms of the cation–anion partial coordination, we observe a slight increase of n^p_{Na}, the values being ~4.0 for Na_3OCl, ~4.3 for $Na_{2.5}OH_{0.5}Cl$ and ~4.6 Na_2OHCl. Correspondingly, the distribution of the structural units given in Table 2 reveals that the percentage of Na atoms fourfold coordinated decreases (from ~70.0% to ~56.9% and ~43.8%, respectively) with a concomitant increase of the fivefold ones (from ~13.8% up to ~30.4% and ~43.7%). The larger number of fivefold Na-centered units at the expense of fourfold ones can be traced back to a concomitant decrease of the number of O_2Cl_2 units (from ~36.6% to ~23.8% and ~13.1%) and a net increase of the O_2Cl_3, O_1Cl_4 and O_3Cl_2 units (the latter from ~0.4% to ~7.1% and ~13.2%).

The behavior of the total and partial coordination numbers of O atoms is worth noticing. n^p_O decreases from ~6.3 in Na_3OCl to ~5.9 and ~5.4 for $Na_{2.5}OH_{0.5}Cl$ and Na_2OHCl, respectively. This decrease is due to a clear increase of lower coordinated units of O at the expense of the higher-coordinated units. Na_2OHCl shows a minimal content of $l = 7$ units and a comparable content of $l = 5$ and $l = 6$ units (~44% *versus* ~45%). The trend in the local environment of O in the hydroxylated phases results from the fact that in $Na_{2.5}OH_{0.5}Cl$ ~52% of O atoms are coordinated only by Na atoms with the remaining having, in addition to Na, one H atom as a neighbor within hydroxyl OH groups. These percentages change in Na_2OHCl to accommodate more H atoms. Regarding Cl atoms the behavior is similar to the one of O atoms after partial replacement of Na by H atoms. In particular, n^p_{Cl} decreases from ~5.7 in Na_3OHCl to ~5.4 and ~4.8, for $Na_{2.5}OH_{0.5}Cl$ and Na_2OHCl, respectively. The amorphous nature of the network favors relatively short Na–Cl distances (~2.75 Å) when compared to those found in the crystalline phase, where each Cl atom is surrounded by twelve Na atoms at a distance of ~3.18 Å.

3.1.5 Structural disorder degree. A deeper insight into the assessment of the structural disorder degree of the three $Na_{3-x}OH_xCl$ compounds is provided by employing the smooth overlap of the atomic positions (SOAP) descriptor.[55,86] SOAP is a well-established mathematical scheme widely used for analyzing the disorder degree in various materials such as amorphous graphene[87] and chalcogenide-based phase-change materials.[88,89] Fig. 7a shows a schematic representation of the SOAP descriptor and Fig. 7b presents the distributions of the absolute value of the SOAP $\mathbf{p}_{Cl}(\mathbf{r})$ vector computed for Na_3OCl from 300 K to 1200 K, along with the comparison to the crystalline phase, and from 300 K to 1000 K for $Na_{2.5}OH_{0.5}Cl$ and Na_2OHCl. Additionally, we provide the average SOAP $\bar{\mathbf{p}}_{Cl}(\mathbf{r})$ value and its standard deviation. For Na_3OCl, the crystalline phase at 300 K exhibits a narrow SOAP $\mathbf{p}_{Cl}(\mathbf{r})$ distribution with $\bar{\mathbf{p}}_{Cl} = 0.55$, with a standard deviation of 0.04. Conversely, amorphous Na_3OCl at 300 K shows a more spread bimodal distribution with

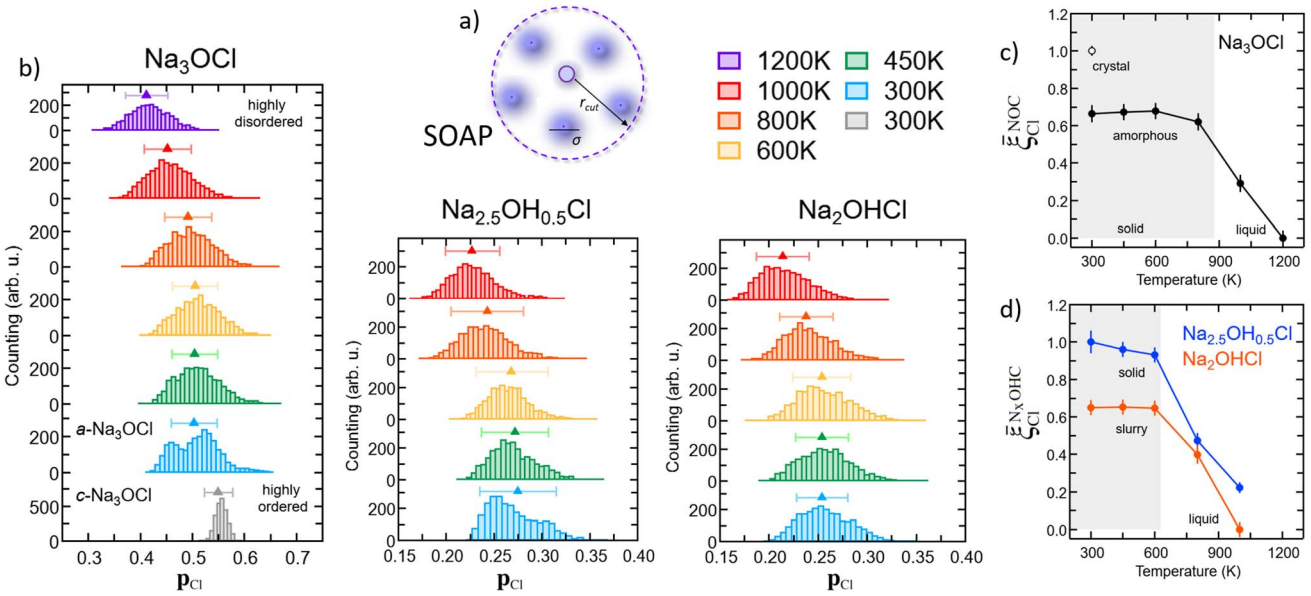

Fig. 7 (Color online) (a) Schematic representation of the SOAP descriptor. (b) Na_3OCl, $Na_{2.5}OH_{0.5}Cl$, and Na_2OHCl SOAP $\mathbf{p}_{Cl}$ distributions computed at different temperatures. The data computed for crystalline Na_3OCl are also reported. Structural disorder degree of the three models framed as SOAP similarity to crystalline Na_3OCl (ξ_{Cl}^{NOC}, (c)) and to the amorphous $Na_{2.5}OH_{0.5}Cl$ phase, ($\xi_{Cl}^{N_xOHC}$, (d)), respectively.

two main peaks (approximately 0.45 and 0.52), an average SOAP $\bar{\mathbf{p}}_{Cl}(\mathbf{r})$ value of 0.5, and a standard deviation of 0.07. As the temperature increases from 300 K to 450 K and up to 800 K, the $\mathbf{p}_{Cl}(\mathbf{r})$ value distributions transition from a bimodal to a symmetrical distribution, while the average SOAP $\bar{\mathbf{p}}_{Cl}(\mathbf{r})$ remains relatively constant up to 800 K (around 0.5). However, at higher temperatures, a noticeable shift towards lower values is observed (approximately 0.45 and 0.40 at 1000 K and 1200 K, respectively), indicating a clear increase in the disordering degree of the system, potentially leading to a phase change (*e.g.*, from solid to liquid). Furthermore, the amorphous $Na_{2.5}OH_{0.5}Cl$ model also exhibits a bimodal SOAP $\mathbf{p}_{Cl}(\mathbf{r})$ distribution at 300 K, although less structured compared to amorphous Na_3OCl, whereas Na_2OHCl shows a more spread SOAP $\mathbf{p}_{Cl}(\mathbf{r})$ distribution. Both $Na_{2.5}OH_{0.5}Cl$ and Na_2OHCl models demonstrate a symmetrical $\mathbf{p}_{Cl}(\mathbf{r})$ distributions from 450 K to 600 K, with a clear shift towards lower averaged $\bar{\mathbf{p}}_{Cl}(\mathbf{r})$ values at temperatures $T \geq 800$ K.

Capitalizing on these insights, for Na_3OCl we have developed similarity metrics (on a ξ_{Cl} scale from 0 to 1) to quantify the degree of disorder with reference to the highly ordered crystalline phase and the highly disordered liquid phase. In Fig. 7c and d, we report the average $\bar{\mathbf{p}}_{Cl}(\mathbf{r})$ as a function of temperature, normalized with respect to the average value of the crystalline phase for Na_3OCl (Fig. 7c), and normalized with respect to the amorphous phase at 300 K for the two hydroxylated phases (Fig. 7d) such as:

$$\bar{\xi}_{Cl}^{NOC} = \frac{\bar{\mathbf{p}}_i - \bar{\mathbf{p}}_{1200\ K}}{\bar{\mathbf{p}}_{cryst} - \bar{\mathbf{p}}_{1200\ K}} \quad (16)$$

and

$$\bar{\xi}_{Cl}^{N_xOHC} = \frac{\bar{\mathbf{p}}_i - \bar{\mathbf{p}}_{1000\ K}}{\bar{\mathbf{p}}_{Na_{2.5}OH_{0.5}Cl300\ K} - \bar{\mathbf{p}}_{1000\ K}} \quad (17)$$

respectively. For the hydroxylated phases the upper bound 1 of the ξ_{Cl} metric is defined by the average $\bar{\mathbf{p}}_{Cl}(\mathbf{r})$ value of $Na_{2.5}OH_{0.5}Cl$ at 300 K, not having at disposal any information related to their crystalline phases and consistently on the basis of the same number of elements and total number of descriptors computed (see Section 2.1). These metrics have enabled us to identify ranges of structural disorder corresponding to its crystalline ($\xi_{Cl}^{NOC} = 1$), amorphous solid ($\xi_{Cl}^{NOC} \sim 0.68$, $\xi_{Cl}^{N_{2.5}OH_{0.5}C} \sim 0.95$ and $\xi_{Cl}^{N_2OHC} \sim 0.65$) and liquid phases ($\xi_{Cl}^{NOC} \leq 0.3$, $\xi_{Cl}^{N_{2.5}OH_{0.5}C} \leq 0.5$ and $\xi_{Cl}^{N_2OHC} \leq 0.4$). It is pertinent to highlight that, at 300 K, the partial substitution of Na ions with H ions leads to heightened disordering, concurrent with a lower temperature threshold for the transition from a solid to a liquid phase (at $T >$ 800 K for Na_3OCl and at $T >$ 600 K for $Na_{3-x}OH_xCl$). Furthermore, at 300 K, the disordering degree exhibited by Na_2OHCl is described as a 'slurry' solid, indicating a significantly lower value when compared to $Na_{2.5}OH_{0.5}Cl$.

3.2 Dynamical properties

3.2.1 Mean square displacements. A first insight into the dynamical properties of amorphous $Na_{3-x}OH_xCl$ is provided by the mean square displacement (defined in Section 2.2 and labeled MSD) of the different ions shown in Fig. 8 at $T = 300$ K. Additional details can be found in Fig. S2 of the ESI.† At $T = 300$ K, Na ions in Na_3OCl are mobile, while the MSD of both Cl and O remains very low. This trend holds at higher temperatures (Fig. S2 of the ESI†), with Na ions reaching over the span of ~50 ps MSD values of ~2.5 Å^2 at $T = 300$ K, ~4 Å^2 at and 450 K, ~15 Å^2 at $T = 600$ K, ~48 Å^2 at $T = 800$ K and ~130 Å^2 at $T = 1000$ K. These results indicate that amorphous Na_3OCl behaves differently from its corresponding defect-free crystalline phase, where Na/Li diffusion is absent due to the lack of disorder induced by the presence of vacancies, as found in crystalline

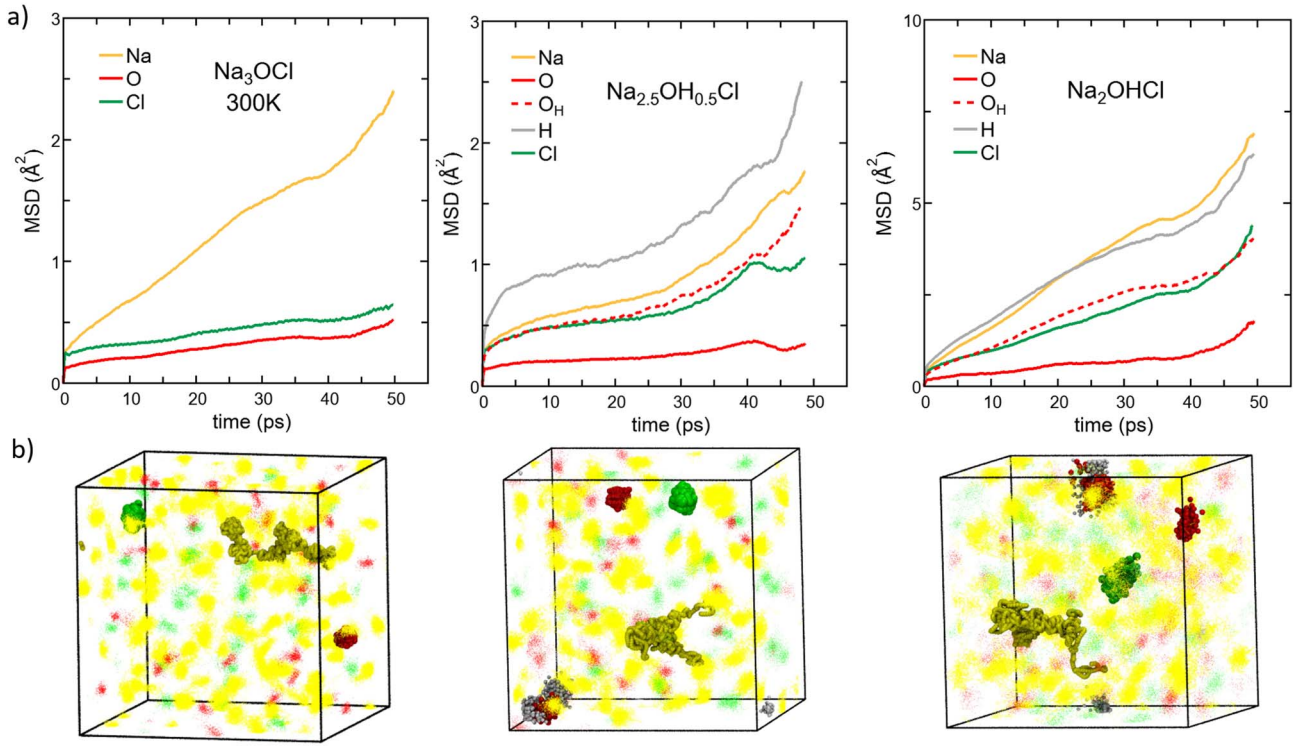

Fig. 8 (Color online) (a) MSD *versus* time for each element in amorphous $Na_{3-x}OH_xCl$ ($x = 0$, $x = 0.5$, and $x = 1$) at $T = 300$ K. Colors legend: Na, yellow; O non-bonded to H atoms, red (solid line); O bonded to H atoms, red (dashed line); H, grey; Cl, green. Note that the MSD calculated at the temperatures $T = 300$ K, $T = 450$ K, $T = 600$ K, $T = 800$ K, and $T = 1000$ K are reported in the ESI (Fig. S1†). (b) Density plots of ~50 ps trajectories of all elements are shown as dots for the three models simulated at 300 K. Na, O, and Cl atom positions are given in yellow, red, and green, respectively. H atoms are omitted for clarity. Examples of an individual local Na migration path and Cl, O and OH local vibrations are highlighted in spheres.

antiperovskites *via* Schottky defect pairs.[90,91] Regarding Cl and O ions, the mobility for both ions at $T = 300$ K is lower than ~1 Å^2, and increases significantly only at very higher temperature ($T \geq 1000$ K) indicating a motion beyond a mere local rearrangement. Heenen and coworkers[25] obtained analogous results for both Cl and O ions; yet, the Cl higher mobility was interpreted as not-negligible and later also termed 'sluggish'.[92]

Different behaviors are recorded in the case of the hydroxylated systems. For both the hydroxylated phases, we reported the MSD data of individual oxygen atoms and those bonded to H atoms (as OH^- anions) separately (corresponding to about ~50% of oxygen atoms in $Na_{2.5}OH_{0.5}Cl$ and only to a small % for Na_2OHCl). At $T = 300$ K, we found that Na and individual O ions in $Na_{2.5}OH_{0.5}Cl$ have MSD values similar to those found in Na_3OCl. The MSD of Cl reaches ~0.9 Å^2 over ~40 ps followed by stabilization, and O atoms involved in OH groups show a MSD value of about ~1 Å^2, whereas H atoms show a steady time increase of the MSD. The enhanced mobility of H atoms can be ascribed to the high rotational dynamical disorder of H atoms around an O atom of a hydroxyl group (see Fig. S3 in the ESI†). Individual O atoms show the least mobility of all, with a MSD stable at ≤0.5 Å^2. This trend is clearly supported by the MSD of $Na_{2.5}OH_{0.5}Cl$ as a function of temperature. Focusing on Na ions at higher temperature, their MSD after ~50 ps is ~1.4 and ~2.0 times larger than the one found in Na_3OCl at 450 K and 600 K, respectively. Therefore, it appears that the presence of H atoms promotes an increase in Na ion mobility at temperatures higher than $T = 300$ K. This occurs also for Cl ions and both O and H involved in OH groups. In contrast, individual O ions (*i.e.* non-bonded to H) are found somewhat less mobile.

To complete our case study and extract a global picture from the behaviour of the mean square displacement, we focus on Na_2OHCl. A first observation from Fig. 8 (rightmost part) reveals that similar trends for the MSD are found. However, OH^- anions boost the MSD of the other species significantly already at room temperature. This effect can be fully appreciated by noting that in Na_2OHCl ~92% of O atoms bind at least one H atom either as OH^- anions or in water molecules. At $T = 300$ K and after ~50 ps, Na ions in Na_2OHCl reached a value of MSD ~3.2 times larger than the one found in Na_3OCl, and with H equally highly mobile and with Cl and O involved in OH groups showing a certain degree of mobility although lower than for Na ions. Individual O atoms show a stable MSD value of ≤3.5 Å^2, indicating mere local vibrations. At 300 K, by considering density plots spanning the 50 picosecond simulation period (Fig. 8b), we observe that atoms other than Na ions only exhibit localized vibrations around central positions. This vibration's extension increases in the order $Na_3OCl < Na_{2.5}OH_{0.5}Cl < Na_2OHCl$, with Na ions showcasing extended migration paths. To enhance comprehension of atom dynamics throughout the

simulation timeframe, we highlighted in Fig. 8b individual local migration paths for Na, Cl, O, and OH in the density plot visualizations. These visualizations further corroborate our MSD-based observations, with Na ions demonstrating extended migration paths. Meanwhile, individual O ions (not involved in OH groups) exhibit highly localized vibrations, and Cl and OH ions show slightly extended vibrations, though consistently localized.

We conclude that all three models at 300 K exhibit solid-state dynamical characteristics. At higher temperature, in Na_2OHCl Na the MSD after ~50 ps is about ~4.5 times larger than the one found in Na_3OCl at 450 K and 600 K. These results indicate, by all means, that the mobility of Na ions is further boosted by the presence of H atoms. Overall, it is evident that Na_3OCl exhibits a consistent profile from 300 K to 800 K, wherein Na ions remain highly mobile with their MSD progressively increasing. In contrast, Cl and O ions stay localized around their initial positions. Notably, these latter two ions begin steady migration only from $T = 1000$ K. In the hydroxylated phases, $Na_{2.5}OH_{0.5}Cl$ and Na_2OHCl, the profiles remain akin to those observed at 300 K up to 600 K. Both Na and H ions experience escalating MSD values, whereas individual O ions (not involved in OH groups) maintain a constant position with minimal vibrations. Remarkably, as Na_2OHCl features only a minor concentration of individual O atoms, we can assert that only a small portion of the model exhibits solid-like behavior up to 600 K. Beyond this temperature, no individual O atoms 'live', as all O atoms are either bonded or interact with H atoms, and the systems behave as a liquid phase. These results are fully consistent with the previous structural analysis based on the SOAP descriptor.

The Na MSD value obtained for Na_2OHCl at 450 K (~21 $Å^2$) is remarkably larger than the one reported by Dawson *et al.*[12] for crystalline Li_2OHCl (~6 $Å^2$ after ~50 ps at $T = 800$ K). What we found for Na_2OHCl differs drastically from what has been reported for crystalline Li_2OHCl antiperovskites, where only rotational dynamics were highlighted for the hydroxyl OH^- groups and no long-range mobility.[12] In this crystalline phase, H atoms are characterized by a constant MSD of ~2 $Å^2$ at $T = 600$ K on a time scale of ~50 ps, whereas the present Na_2OHCl model features an increase of the MSD to a value of ~60 $Å^2$ after ~50 ps at $T = 600$ K (Fig. S2 in the ESI†).

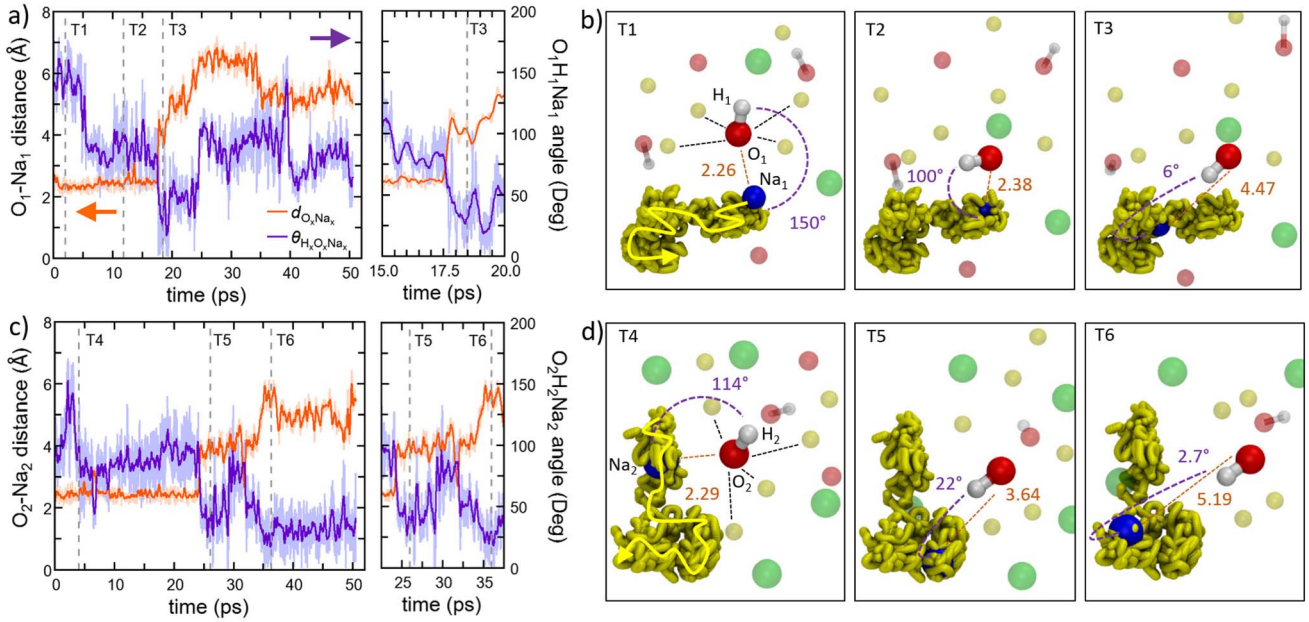

Fig. 9 (Color online) Proposed paddlewheel dynamics monitored in amorphous $Na_{2.5}OH_{0.5}Cl$ at 300 K. We show the temporal evolutions of two distinct scenarios involving different atoms. (a and c) The interatomic distance between an O atom (O_1 and O_2) of one hydroxyl group and a coordinated Na atom (Na_1 and Na_2) and the HONa angles ($H_1O_1Na_1$ and $H_2O_2Na_2$) along the ~50 ps trajectory. Light orange and purple lines correspond to the instantaneous interatomic distance $d_{O_xNa_x}$ and $\theta_{H_xO_xNa_x}$ angle, whereas the strong lines correspond to the sliding average with a window of 0.1 ps. (b and d) Atomistic views of the temporal frames Ty ($y = 1$–6) indicated in (a) and (b). In (b), between 0 and 5 ps, a sixfold coordinated O_1 atom of one hydroxyl group shows a bonding distance of 2.26 Å with the Na atom labelled Na_1 and an HONa angle of ~150° (T1). At 5 ps, the hydroxyl OH bond is rotating with respect to Na_1 (from ~150° to ~100°) while maintaining a distance O_1–Na_1 equal to 2.38 Å. This scenario lasts up to 17 ps (T2). After 17.5 ps and up to 25 ps a further rotation of the OH group bringing the corresponding angle from ~100° to ≤50° (~6° at T3) induces the displacement of the Na_1 atom to a larger distance (>4.5 Å) escaping the first coordination shell of the O_1 atom. In (d) between 4 and 23 ps, a sixfold coordinated O_2 atom of one hydroxyl group shows a bonding distance of 2.29 Å with the Na atom labelled Na_2 and an HONa angle of 90°–120° (T4). At 26 ps, the hydroxyl OH bond is rotating with respect to Na_2 (to ≤50°) inducing the displacement of the Na_2 atom to a larger distance (>3.6 Å) escaping the first coordination shell of the O_2 atom (T5). A further rotation to 3° is accompanied by a displacement of the Na_2 atom to a larger distance (>5 Å, T6). The surrounding atoms of O_1 and O_2 at a distance lower than >5 Å are shown in transparent color. Dashed lines indicate the atoms coordinated within the first coordination shell of O_1 and O_2 (<3.3 Å). The concerted migration pathways of Na_1 and Na_2 atoms along the ~50 ps trajectory are shown in transparent dark yellow. As a guide, an arrow is added to indicate the direction of the pathway. Color legend: Na atoms, yellow; O atoms, red; Cl atoms, green; H atoms, white; Na_1 and Na_2 atoms at Ty points are shown in blue.

3.2.2 The paddlewheel effect. We have found that the mobility of Na ions in $Na_{3-x}OH_xCl$ is strictly related to the presence of hydroxyl OH^- anions. An important relationship between the Na-ion transport mechanism and O–H rotation effects in these systems has been reported by Song *et al.*[93] and Howard *et al.*[94] These studies demonstrate that the rapid rotation of O–H bonds leads to the creation of empty space promoting the formation of defects, which, in turn, are crucial for achieving fast, correlated Na-ion transport. The rotational disorder due to the hydroxyl OH^- anions, along with other anions, is a feature common to other solid electrolytes, such as crystalline Na_3OBH_4[13] and $Na_{3-x}O_{1-x}(NH_2)_x(BH_4)$.[95] Ion migration occurs *via* a mechanism that combines the concerted motion of ions with large quasi-permanent reorientations of the surrounding hydroxyl groups. This latter effect, known as the paddlewheel mechanism,[30,96,97] is typically observed in high-temperature crystalline polymorphs.[98]

Unlike in crystalline materials, the paddlewheel dynamics in glassy matrices can contribute to the ion mobility also at room temperature,[30] *via* the strong coupling between the rotational motion of the anions and the translational motion of the alkaline cations.[30,96,98] Based on the above analyses, we propose that H-containing amorphous $Na_{3-x}OH_xCl$ compounds show three distinct features that facilitate the occurrence of paddlewheel dynamics. The degree to which these dynamics manifest themselves is temperature-dependent. First, these systems contain hydroxyl groups which are free to rotate, impacting the neighbouring cations. Second, the amorphous matrix has a lower density than its crystalline counterpart that makes available additional free volume for O–H rotations, facilitating

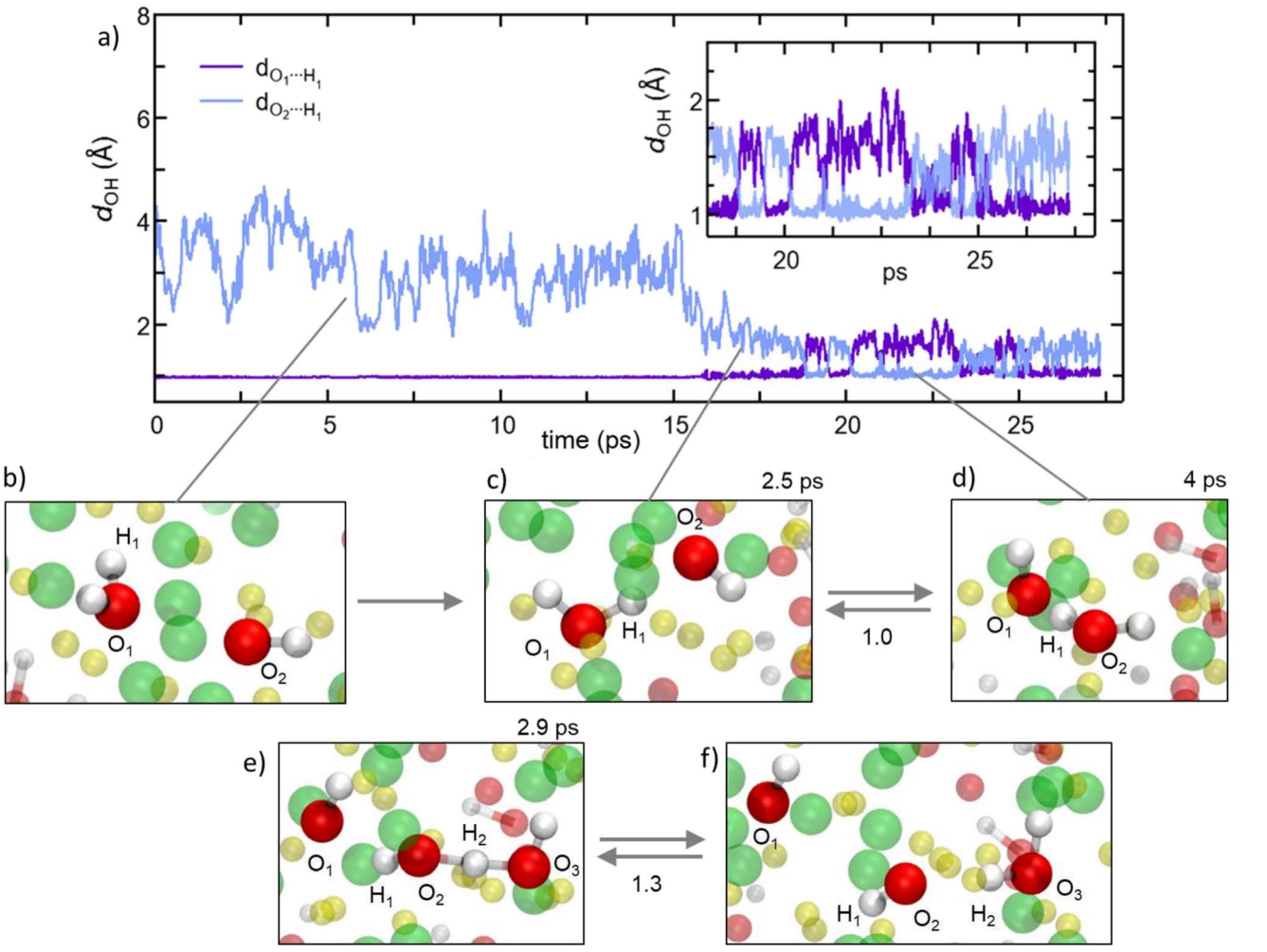

Fig. 10 (Color online) For the Na_2OHCl system: the proton hopping process by which H atoms migrate through a dynamical switch between σ and hydrogen bonds giving rise to the formation of metastable water molecules (*i.e.* Grotthuss-like mechanism).[80–85] (a) Temporal evolution of the interatomic distance between one H atom labelled H_1 atom, belonging to a water molecule initially formed, and its bonded O atom labelled O_1. Also shown is the temporal evolution of the distance between H_1 and a second O atom labelled O_2 that is part of a neighboring hydroxyl group. Inset: zoomed-in view of the temporal window along which H_1 is shared between two O_1 and O_2, leading to the transient formation and breaking of the OH bond and water molecules. (b–f) Inter-unit transitions between structural units in amorphous Na_2OHCl at 300 K. Indicatively, the mean lifetimes of the transient H-bonds and water molecules are reported on top of the panels, whereas the transition rates are reported between the panels. Here, the transition rate is defined as the number of inter-unit transitions per ps observed within a given process (H-bond or water molecule formation). Color legend: Na, yellow; O, red; Cl, green.

anion reorientations. Third, while it is typical for most glasses to exhibit a lower density compared to their crystalline form, amorphous $Na_{3-x}OH_xCl$ systems have a potentially unusual characteristic – the absence of covalent bonding in their atomic structure. These features are found in strong accordance with the features of paddlewheel dynamics reported for $75Li_2S$-$25P_2S_5$ glass.[30]

A more detailed view of the dynamical mechanism is shown in Fig. 9a–d. These panels illustrate the rotation of two hydroxyl (OH) groups nearest neighbor to one sodium (Na) ion during Na migration. Throughout the entire process, O(OH) and Na maintain their coordination of six cations and four-to-five anions, respectively. The coordination of Na is preserved by means of rotational displacements of the anion through a paddlewheel-type mechanism. Another salient feature observed in these migration events is the dissociation or undocking of Na from a subset of its neighboring anions at the onset of the process, followed by its association or docking to new anions towards the end.[30]

Former experimental and computational results have also stirred a debate about the formation of water molecules in antiperovskites. Based on the analysis presented above, $Na_{2.5}OH_{0.5}Cl$ appears not to show any water formation since all H atoms are bound in OH groups, while our Na_2OHCl model system does, with ~9.3% of O atoms involved in H_2O molecules. The formation of these water molecules can be elucidated by , as shown in Fig. 10a, a typical H hopping process involving OH groups in Na_2OHCl at $T = 300$ K. We first show the temporal evolution of two representative distances. The first is the one between the H atom termed H_1 belonging to a water molecule, previously formed, and the O atom termed O_1 atom to which it is bonded ($d_{O_1H_1}$, initially at ~0.98 Å). The second one concerns the same H_1 atom and a second O atom termed O_2 atom belonging to a neighbouring OH group ($d_{O_2H_1}$, initially at ~3.8 Å; Fig. 10b). After about ~15 ps, H_1 starts to form a strong hydrogen bond (H-bond) with the neighbouring O_2 atom of one OH hydroxyl group at a distance of ~1.9 Å. The mean lifetime of this transient H-bond is ~2.5 ps. Then, H_1 is shared between O_1 and O_2 *via* forming and breaking O–H bonds showing an average $d_{O_{1,2}H_1}$ distance of ~1.6 Å and forming eventually a water molecule upon H transfer (Fig. 10c and d). Its transition rate, defined as the number of inter-unit transitions per ps observed within a given process (H-bond or water molecule formation), is of about 1.0 before the formation of a stable new H_2O molecule. In Fig. 10 panels (e–f) exemplify the dynamical evolution of the previous environment toward H transfer to a third hydroxyl group (from O_2 to O_3), resulting in the formation of a new water molecule. The presented mechanism is very similar to the known Grotthuss one,[80–85] in which the H atom switches between a σ bond and a hydrogen bond to propagate and eventually stabilize in a newly formed water molecule, as in proton-conducting solid-oxide materials.

3.2.3 Ions diffusion. The long-range mobility of alkaline ions in a solid-state electrolyte can be assessed by considering the log–log plot of the MSD (eqn (3) *vs.* t for the temperatures of interest (see Fig. 11). Several regimes are noticeable as a function of time, especially at $T = 300$ K in our case. The initial part

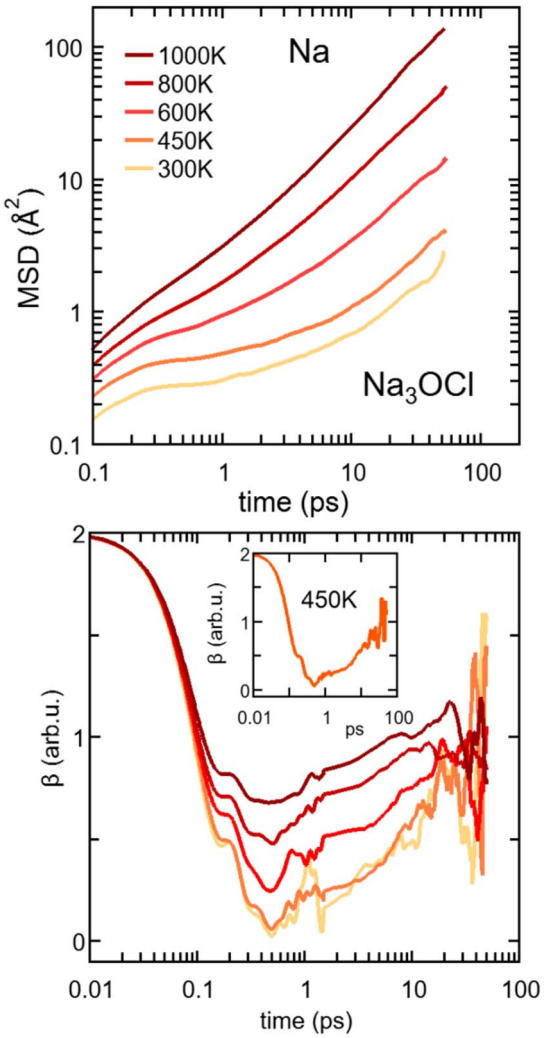

Fig. 11 (Color online) Top: log–log plot of MSD *vs.* time for Na in Na_3OCl at temperatures in between $T = 300$ K and 1200 K. Bottom: corresponding values of β. Inset: β value as a function of time at $T = 800$ K. Note that the log–log plots of MSD *vs.* time data for the $Na_{3-x}OH_xCl$ ($x = 0$, $x = 0.5$, and $x = 1$) systems are reported in the ESI (Fig. S2†).

consists of a ballistic regime with the MSD showing a quadratic dependence on time. With increasing t, a plateau is attained corresponding to the so-called caging regime with Na ions trapped in a very limited portion of space by the nearest neighbors. In Na_3OCl, the cage regime clearly persists up to ~1 ps at $T = 300$ K and ~0.8 ps at $T = 450$ K, while it does not manifest itself at higher temperatures. Then, the diffusive regime for Na atoms sets in at longer times with Na ions moving along preferential paths. Under these conditions, the MSD takes a linear dependence on time and the ion self-diffusion coefficients (D^*) can be obtained *via* the Einstein equation (eqn (5)) at different temperatures.

The onset of the diffusive regime can be monitored *via* the time behaviour of β (eqn (4)), given in Fig. 11 for Na_3OCl. As expected, the higher the temperature the faster the β approaches ~1, *i.e.* at $T = 450$ K, 600 K, 800 K, and 100 K and

this target value is reached after ~33 ps, ~23 ps, ~15 ps, and ~8 ps respectively. At 300 K, the diffusive regime is not reached within ~50 ps, the behaviour of β being affected by statistical noise for increasing time. Analogous information on the MSD of the two hydroxylated systems is given in Fig. S2, ESI† (linear plot) and Fig. S4, ESI† (log–log plot, as in Fig. 11). Remarkably, for $T \leq 450$ K, the cage regime disappears for $Na_{2.5}OH_{0.5}Cl$ and Na_2OHCl. This is consistent with the boosted Na ion dynamics due to the OH anion rotational mechanism discussed before. Also, the MSD trend of H atoms features high values at short times (<~1 ps) for any given temperature, again due to the rotational disordered of OH anions. At longer times, the MSD profiles of H and Na atoms do superpose as a result of a fully enhanced diffusive behavior concerning all Na and OH groups.

Having identified the temperatures at which Na ions reached the diffusive regime (range 450 K–800 K for Na_3OCl and 300 K–600 K for $Na_{2.5}OH_{0.5}Cl$ and Na_2OHCl), we calculated for the three systems the self-diffusion coefficients (tracer, D^*) for Na by using the Einstein equation (eqn (5)) and then converted them into Na-ion conductivities with eqn (7). By plotting these data according to the relationship $\log D^*$ *vs.* $1000/T$ (Fig. 12) and fitting it in the Arrhenius form, we obtain by extrapolation the uncorrelated tracer conductivity σ^* of Na ions at $T = 300$ K, as customarily done for crystalline solid-state electrolytes.[7,12] D^* and σ^* values are reported in Table 3, together with the calculated activation energy (E_a) of Na ion transport. We have also computed the tracer diffusion coefficient (D^*) for the least mobile element, namely individual O atoms, at 300 K for all three models. The calculated values are 1.7×10^{-7} cm^2 s^{-1}, 1.5×10^{-7} cm^2 s^{-1}, and 3.9×10^{-7} cm^2 s^{-1} for the three respective models. Notably, these values are lower by two orders of magnitude than the typical diffusion coefficients observed in liquids (~10^{-5} cm^2 s^{-1}),[42] thus providing additional reinforcement to the previous observations that underline the solid-like nature of the three models at 300 K.

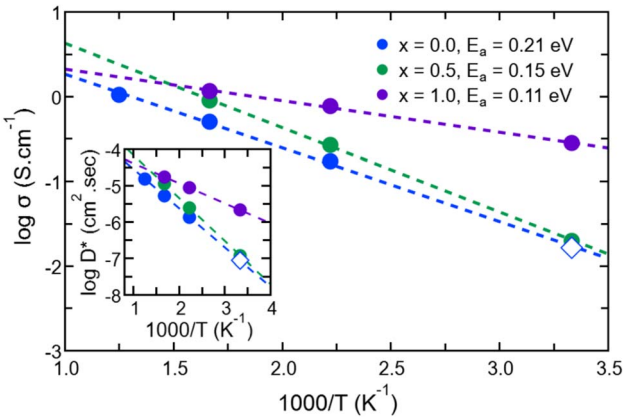

Fig. 12 (Color online) Na-ion self-diffusion coefficients (inset) and conductivities of amorphous $Na_{3-x}OH_xCl$ ($x = 0$, $x = 0.5$, and $x = 1$). We also report the activation energies of Na ionic conduction obtained *via* a linear Arrhenius fit. Closed circles correspond to FPMD data and open circles correspond to data at $T = 300$ K extrapolated by using the linear Arrhenius fit.

Table 3 Na tracer diffusion coefficients (D^*), Na ion tracer (σ^*), charge (σ^σ) and total conductivities (σ^{tot}), activation energies (E_a) and Haven ratio ($H_R^{J,tot}$) extrapolated at $T = 300$ K and directly computed at $T = 450$ K on the basis of FPMD simulations. We report the values for the three $Na_{3-x}OH_xCl$ ($x = 0$, $x = 0.5$, and $x = 1$) models

	T (K)	$x = 0$	$x = 0.5$	$x = 1.0$
D^* (cm^2 s^{-1})	300 K[a]	8.65×10^{-8}	1.20×10^{-7}	2.13×10^{-6}
σ^* (S cm^{-1})	300 K[a]	0.016	0.08	0.28
E_a (eV)	300 K	0.21	0.15	0.11
D^* (cm^2 s^{-1})	450 K	1.36×10^{-6}	2.47×10^{-6}	8.74×10^{-6}
σ^* (S cm^{-1})	450 K	0.17	0.27	0.77
σ_{ion} (S cm^{-1})	450 K	0.08	0.10	0.22
σ_{ion}^{tot} (S cm^{-1})	450 K	0.67	0.75	0.99
H_R^σ	450 K	2.03	2.67	3.50
H_R^{tot}	450 K	0.89	1.84	2.51

[a] Data extrapolated at $T = 300$ K.

3.2.4 Ionic conductivity and correlation effects. In terms of conductivity σ^*, we obtained at 300 K a value of ~16 mS cm^{-1} for Na_3OCl and a E_a value of Na ion transport of 0.21 eV. The σ^* value obtained is two order of magnitude larger of the ~0.2 mS cm^{-1} obtained by Dawson *et al.* at 500 K (ref. 7), showing a similar E_a calculated for defected crystalline Na_3OCl.[1,17] For this model, we also computed the energy barrier E_a of Na ions during migration through distinct anion pairs, namely OO, ClCl, and OCl, within the Na_3OCl model through static transition calculations, as commonly performed for crystalline systems.[15] The outcomes of our computations reveal energy barrier values of 0.23 eV, 0.41 eV, and 0.73 eV, respectively, for the aforementioned anion pairs (Fig. S5 within the ESI†). This analysis underscores a significantly higher favorability for migration *via* the OO pair, in contrast to the ClCl and OCl pairs. It is noteworthy that the minimum energy barrier obtained, which corresponds closely to the value of 0.21 eV obtained from Arrhenius fitting of self-diffusion and conductivity data, supports the consistency and validity of our findings. While we acknowledge that the static calculations do not take into account the influence of thermal motion and collective dynamics, their alignment with the Arrhenius fitting outcomes adds weight to the support they provide. It is worth mentioning that, due to the intricate nature of OH rotational dynamics as the main promoter of Na migration in the hydroxylated models, similar static calculations have not been performed for these two compounds as these aspects are better assessed by following the Arrhenius fitting of self-diffusion and conductivity processes extracted from FPMD trajectories.

For $Na_{2.5}OH_{0.5}Cl$ and Na_2OHCl, we obtained at 300 K $E_a = 0.15$ eV, $E_a = 0.11$ eV and a Na tracer conductivity equal to ~80 mS cm^{-1} and ~280 mS cm^{-1}, respectively. These data demonstrate that Na ion transport is promoted by the addition of H atoms. These values correspond to the ideal case where no collective effects are taken into account, as those due to alike-Na ions or different ions. However, since these effects are present in experiments, it is appropriate to account for them by considering the so-called Haven ratio (H_R) which can be obtained *via* eqn (9) and (10) in order to quantify the contribution

of alike-Na ions (H_R^{σ})[66–68,71] or a total contribution coming from all positive and negative ions (H_R^{tot}, eqn (11)).[61]

Often, previous studies on crystalline Li/Na antiperovskites assumed a Haven ratio equal to 1 disregarding collective effects.[7,12] While single-ion conducting glasses typically exhibit Haven ratios of ~0.1–0.6 indicative of positive correlating effects,[60,99] ionic liquids[61] and molten salts[62] behave oppositely with H_R values larger than 1. For comparison, in Table 3 we report the values of H_R^{σ}, H_R^{tot} and the corresponding Na and total conductivities obtained at $T = 450$ K. We obtained H_R^{σ} values larger than 1, indicating a strong negative effect of the collective correlations of alike-Na ions. Therefore, at this temperature, the behaviour of amorphous $Na_{3-x}OH_xCl$ systems in terms of conductivity is closer to ionic liquids and molten salts than to a glassy matrix. We also remark that this specific effect is more important when Na is partially replaced by H (from 2.0 for Na_3OCl to 2.7 and 3.5 for the two hydroxylated phases). Finally, the resulting Na charge conductivities (σ_{ion}) are lower than the uncorrelated Na tracer conductivity σ^* for the three systems.

In terms of H_R^{tot}, we obtained for Na_3OCl a much lower value than H_R^{σ} (0.89 *vs.* 2.03), which indicates significant positive collective correlated effects when the mobility of all ions is taken into consideration. The value obtained for Na_3OCl is found close to the typical values found for single-ion conducting glasses.[60,99] This is not the case for the two hydroxylated models, which showed values always larger than 1 for H_R^{tot} meaning that in the presence of H (OH hydroxyl groups) negative effects are more important. The corresponding final total ionic conductivities (σ_{ion}^{tot}) are moderately larger to the Na ions uncorrelated tracer ionic conductivity (σ^*) estimation for the three models Na_3OCl (0.67 *vs.* 0.17 S cm^{-1}), $Na_{2.5}OH_{0.5}Cl$ (0.75 *vs.* 0.27 S cm^{-1}), and Na_2OHCl (0.99 *vs.* 0.77 S cm^{-1}). The σ_{ion}^{tot} obtained here at 450 K is finally found 1.5 times higher in Na-deficient Na_2OHCl than Na_2OHCl, whereas in the case of Na_2OHI/Na_2OHI an increase of 10^2 times at about 550 K was reported.[100]

Therefore, the Na ionic conductivity of disordered $Na_{3-x}OH_xCl$ systems can be a viable, effective alternative to the crystalline counterparts, with the partial replacement of Na with H enhancing ion transport. However, the mobility of the other ions (Cl, O, and H) is concomitantly boosted which might be detrimental to practical electrolyte applications.

4 Conclusions

X_3OA-based antiperovskites have shown promising potential as solid-state electrolytes for ion batteries due to their structural and dynamical properties. However, while the structure and ion dynamics mechanisms of crystalline X_3OA compounds are well-known, there is a lack of quantitative structural characterization for amorphous antiperovskites. In this study, we used first-principles molecular dynamics to quantitatively assess the structure and ion dynamics mechanisms of three amorphous $Na_{3-x}OH_xCl$ (with $x = 0$, 0.5, and 1) Na-rich antiperovskites. We found that amorphous Na_3OCl shows a substantially different structure compared to its crystalline counterpart, with a disordered structure exhibiting limited intermediate range order and short-range order driven by a majority of four-fold Na atoms (~70%), in terms of counter-ion coordination by means of ionic bonds. Na–O bond distances are close to those reported in the crystalline phase, while Na–Cl distances are significantly shorter. As a result, a reduced number of neighboring counter-ions and Na atoms are favored in the local surrounding of Na atoms in the amorphous phase. Na is found primarily coordinated to both anions (O and Cl), with only a small percentage of Na atoms coordinated exclusively to O or Cl atoms. These results unveil contrasting differences in the structure of amorphous Na_3OCl compared to previous models conjectured for glassy Li_3OCl, which was based on the segregation of Li_2O and LiCl-rich regions.

The partial replacement of Na atoms with H in the two hydroxylated phases studied ($Na_{2.5}OH_{0.5}Cl$ and Na_2OHCl) gives rise to a lower degree of structural organization when compared to H-free Na_3OCl, with all H atoms bonded to O atoms. At 300 K, the partial substitution of Na ions with H precipitates a heightened disordering degree concurrent with a lower temperature threshold for the solid-to-liquid transition. Particularly, Na_2OHCl exhibits a disordering degree we characterize as 'slurry', owing to a degree to be significantly greater with respect to $Na_{2.5}OH_{0.5}Cl$. Amorphous Na_3OCl has a unique microscopic structure that enables remarkable Na ion dynamics and ionic conductivity, challenging that of defective crystalline phases. The presence of hydroxyl OH^- anions in the hydroxylated models is crucial for the mobility of Na ions, which is enhanced by rapid rotation of O–H bonds and paddlewheel-type mechanisms. This promotes the formation of available space, which is essential for achieving fast Na-ion transport. Interestingly, the paddlewheel dynamics in the hydroxylated models of glassy matrices can contribute to ion mobility even at room temperature, owing to the strong coupling between the rotational motion of the anions and the translational motion of the alkaline cations. In terms of correlated dynamical effects, the behaviour of amorphous Na_3OCl is found closer to that of single-ion conducting glasses, whereas the two hydroxylated models are found closer to ionic liquids and molten salts than to a glassy matrix. We also observe a noticeable shift in favor of positive correlated effects for Na_3OCl, whereas for the two hydroxylated phases negative effects are more important.

Concerning the presence of water molecules in antiperovskites, our study proves that the presence of H atoms promotes the formation of H-bonds in $Na_{2.5}OH_{0.5}Cl$, while only in the case of Na_2OHCl the formation of a small amount of water is observed.

Overall, the results obtained in this work add to the growing evidence that disordered Na-rich antiperovskites provide a viable and effective alternative to their crystalline counterparts as solid state electrolytes. Our results underscore the significance of conducting quantitative structural assessments to better comprehend the impact of the structure on the performances of these systems.

Data availability

Representative trajectory files of the three $Na_{3-x}OH_xCl$ models are available at the European Center of Excellence Novel Materials Discovery (CoE-NOMAD) repository.[101]

Author contributions

Tan-Lien Pham: investigation, writing, and formal analysis. Mohammed Guerboub: investigation, writing, and formal analysis. Assil Bouzid: methodology and writing. Carlo Massobrio: methodology and writing. Mauro Boero: methodology and writing. Young-Han Shin: conceptualization, supervision, investigation, and writing. Guido Ori: conceptualization, supervision, investigation, and writing.

Conflicts of interest

There are no conflicts to declare.

Acknowledgements

This work was supported by the National Research Foundation of Korea (NRF) grants funded by the Ministry of Science and ICT (MSIT), government of South Korea (grant no. 2021R1F1A1048555). We acknowledge financial support from the Agence National de la Recherche (ANR) within the framework of the project AMSES No. ANR-20-CE08-0021, the Seed Money program (project MEDIA) of Eucor-The European Campus, the Interdisciplinary Thematic Institute QMat, as part of the ITI 2021–2028 program of the University of Strasbourg, CNRS and Inserm. This project has also received funding from the European Union's Horizon 2020 research and innovation programme under the Marie Skłodowska-Curie grant agreement number 847471 (QUSTEC). Calculations were performed by using resources from GENCI (Grand Equipement National de Calcul Intensif, grant no. A0100807670, A0120807670, and A0140807670) and the Pole HPC Équipe@Meso of the Université de Strasbourg.

References

1 J. Dawson, T. Famprikis and K. Johnston, *J. Mater. Chem.*, 2021, **9**, 18746–18772.
2 W. Xia, Z. Yang, Z. Feipeng, A. Keegan, Z. Ruo, L. Shuai, Z. Ruqiang, Z. Yusheng and S. Xueliang, *Chem. Rev.*, 2022, **122**, 3763–3819.
3 T. Shao, C. Liu, W. Deng, C. Li, X. Wang, M. Xue and R. Li, *Batteries Supercaps*, 2019, **2**, 403–427.
4 K. Kim, Y. Li, P. Tsai, F. Wang, S. Son, Y. Chiang and D. Siegel, *Chem. Mater.*, 2022, **34**, 947–958.
5 K. Yang, D. Liu, Z. Qian, D. Jiang and R. Wang, *ACS Nano*, 2021, **15**, 17232–17246.
6 Y. Zhao and L. L. Daemen, *J. Am. Chem. Soc.*, 2012, **134**, 15042–15047.
7 B. Goldmann, M. Clarke, J. Dawson and M. Islam, *J. Mater. Chem. A*, 2022, **10**, 2249–2255.
8 H. Fang and P. Jena, *Proc. Natl. Acad. Sci. U.S.A.*, 2017, **114**, 11046–11051.
9 Z. Deng, D. Ni, D. Chen, Y. Bian, S. Li, Z. Wang and Y. Zhao, *InfoMat*, 2022, **4**, 2567–3165.
10 W. Yonggang, Q. Wang, Z. Liu, Z. Zhou, S. Li, J. Zhu, R. Zou, Y. Wang, J. Lin and Y. Zhao, *J. Power Sources*, 2015, **293**, 735–740.
11 J. Oh, L. He, B. Chua, K. Zeng and L. Lu, *Energy Stor. Mater.*, 2021, **34**, 28–44.
12 J. Dawson, H. Chen and M. Islam, *J. Phys. Chem. C*, 2020, **122**, 23978–23984.
13 E. Ahiavi, J. Dawson, U. Kudu, M. Courty, M. Islam, O. Clemens, C. Masquelier and T. Famprikis, *J. Power Sources*, 2020, **471**, 228489.
14 X. Xu, K. S. Hui, K. N. Hui, H. Wang and J. Liu, *Mater. Horiz.*, 2020, **7**, 1246–1278.
15 T.-L. Pham, W. I. Choi, A. Shafique, H. J. Kim, M. Shim, K. Min, W.-J. Son, I. Jang, D. S. Kim, M. Boero, C. Massobrio, G. Ori, H. S. Lee and Y.-H. Shin, *Phys. Rev. Appl.*, 2023, **19**, 034004.
16 S. Gao, C. Tassel, S. Fujii, H. Ubukata, T. Zhu, D. Zhang, T. Broux, T. Saito, C. Zhong, E. Yoruk and K. Yamamoto, *Chem. Mater.*, 2022, **34**, 6815–6823.
17 J. Zheng, B. Perry and Y. Wu, *ACS Mater. Au*, 2021, **1**, 92–106.
18 M. H. Braga, N. S. Grundish, A. J. Murchison and J. B. Goodenough, *Energy Environ. Sci.*, 2017, **10**, 331–336.
19 M. H. Braga, J. A. Ferreira, V. Stockhausen, J. E. Oliveira and A. El-Azab, *J. Mater. Chem. A*, 2014, **2**, 5470–5480.
20 M. H. Braga, A. J. Murchison, J. A. Ferreira, P. Singh and J. B. Goodenough, *Energy Environ. Sci.*, 2016, **9**, 948–954.
21 M. H. Braga, J. A. Ferreira, A. J. Murchison and J. B. Goodenough, *J. Electrochem. Soc.*, 2017, **164**, A207–A213.
22 I. Hanghofer, G. J. Redhammer, S. Rohde, I. Hanzu, A. Senyshyn, H. M. R. Wilkening and D. Rettenwander, *Chem. Mater.*, 2018, **30**, 8134–8144.
23 D. A. Steingart and V. Viswanathan, *Energy Environ. Sci.*, 2018, **11**, 221–222.
24 J. T. Frith, M. J. Lacey and U. Ulissi, *Nat. Commun.*, 2023, **14**(1), 420.
25 H. H. Heenen, J. Voss, C. Scheurer, K. Reuter and A. C. Luntz, *J. Phys. Chem. Lett.*, 2019, **10**, 2264–2269.
26 Y. W. Choi, C. M. Araujo and R. Lizarraga, *J. Power Sources*, 2022, **521**, 230916.
27 Y. Tian, F. Ding, H. Zhong, C. Liu, Y.-B. He, J. Liu, X. Liu and Q. Xu, *Energy Stor. Mater.*, 2018, **14**, 49–57.
28 Y. Tian, F. Ding, L. Sang, Y. He, X. Liu and Q. Xu, *Int. J. Electrochem. Sci.*, 2019, **14**, 4781–4798.
29 Y. Gao, S. Sun, X. Zhang, Y. Liu, J. Hu, Z. Huang, M. Gao and H. Pan, *Adv. Funct. Mater.*, 2021, **31**, 2009692.
30 J. G. Smith and D. J. Siegel, *Nat. Commun.*, 2020, **11**, 1483.
31 W. Xia, Y. Zhao, F. Zhao, K. Adair, R. Zhao, S. Li, R. Zou, Y. Zhao and X. Sun, *Chem. Rev.*, 2022, **112**, 3763–3819.
32 In the present manuscript we use the formula $Na_{3-x}OH_xCl$ to denote the hydroxylated phases in accordance with the widely accepted and commonly used in the community and literature to describe this type of compound (see for instance ref. 1, 2, 12, 16 and 33).
33 L. Gao, P. Jiangyang, D. Longbang, Z. Jinlong, W. Liping, G. Song, Z. Ruqiang, K. Le, H. Songbai and Y. Zhao, *Chin. J. Chem.*, 2023, **42**, 100048.

34 R. Car and M. Parrinello, *Phys. Rev. Lett.*, 1985, **55**, 2471–2474.
35 J. Perdew, K. Burke and M. Ernzerhof, *Phys. Rev. Lett.*, 1996, **77**, 3865.
36 N. Troullier and J. L. Martins, *Phys. Rev. B: Condens. Matter Mater. Phys.*, 1991, **43**, 1993–2006.
37 S. Nosé, *Mol. Phys.*, 1984, **52**, 255–268.
38 S. Nosé, *J. Chem. Phys.*, 1984, **81**, 511–519.
39 W. G. Hoover, *Phys. Rev. A*, 1985, **31**, 1695–1697.
40 G. J. Martyna, M. L. Klein and M. Tuckerman, *J. Chem. Phys.*, 1992, **97**, 2635–2643.
41 P. Blochl and M. Parrinello, *Phys. Rev. B: Condens. Matter Mater. Phys.*, 1992, **45**, 9413–9416.
42 C. Massobrio, *The Structure of Amorphous Materials Using Molecular Dynamics*, IOP Publishing, 2022.
43 A. Bouzid, T. Pham, Z. Chaker, M. Boero, C. Massobrio, Y. Shin and G. Ori, *Phys. Rev. B*, 2021, **103**, 094204.
44 G. Ori, A. Bouzid, E. Martin, C. Massobrio, S. L. Roux and M. Boero, *Solid State Sci.*, 2019, **95**, 105925.
45 G. Ori, C. Massobrio, A. B. M. Boero and B. Coasne, *Phys. Rev. B: Condens. Matter Mater. Phys.*, 2014, **90**, 045423.
46 Q. Evrard, Z. Chaker, M. Roger, C. M. Sevrain, E. Delahaye, E. Gallart, M. Gilliot, P. C. Leuvrey, J.-M. Rueff, P. Rabu, M. Boero, C. Massobrio, G. Ori and G. Rogez, *Adv. Funct. Mater.*, 2017, **27**, 1703576.
47 Z. Chaker, G. Ori, M. Boero and C. Massobrio, *Beilstein J. Nanotechnol.*, 2018, **8**, 857–860.
48 Z. Chaker, A. Bouzid, B. Coasne, C. Massobrio, M. Boero and G. Ori, *J. Non-Cryst. Solids*, 2018, **498**, 288–293.
49 G. Cotin, C. Kiefer, F. Perton, M. Boero, B. Ozdamar, A. Bouzid, G. Ori, C. Massobrio, D. Begin, B. Pichon, D. Mertz and S. Begin-Colin, *ACS Appl. Nano Mater.*, 2018, **1**, 4306–4316.
50 B. Ozdamar, A. Bouzid, G. Ori, C. Massobrio and M. Boero, *J. Chem. Theory Comput.*, 2018, **14**, 225–235.
51 D. Gentili and G. Ori, *Nanoscale*, 2022, **14**, 14385–14432.
52 D. Gentili, G. Ori, L. Ortolani, V. Morandi and M. Cavallini, *ChemNanoMat*, 2017, **3**, 874–878.
53 K. Hippler, S. Sitta, P. Vogt and H. Sabrowsky, *Acta Crystallogr.*, 1990, **463**, 736–738.
54 *CPMD, Copyright 1990–2023 by IBM Corp. and 1994–2001 by Max Planck Institute, Stuttgart*, **https://github.com/CPMD-code**.
55 S. De, A. P. Bartók, G. Csányi and M. Ceriotti, *Phys. Chem. Chem. Phys.*, 2016, **18**, 13754–13769.
56 V. L. Deringer, A. P. Bartók, N. Bernstein, D. M. Wilkins, M. Ceriotti and G. Csányi, *Chem. Rev.*, 2021, **121**, 10073–10141.
57 L. Himanen, M. O. Jäger, E. V. Morooka, F. F. Canova, Y. S. Ranawat, D. Z. Gao, P. Rinke and A. S. Foster, *Comput. Phys. Commun.*, 2020, **247**, 106949.
58 *Molecular Dynamics Simulations of Disordered Materials*, ed. C. Massobrio, J. Du, M. Bernasconi and P. Salmon, Springer International Publishing, Cham, 2015.
59 *Theory and Simulation in Physics for Materials Applications: Cutting-Edge Techniques in Theoretical and Computational Materials Science*, ed. E. Levchenko, Y. Dappe and G. Ori, Springer International Publishing, Cham, 2020.
60 J. Habasaki, *Int. J. Appl. Glass Sci.*, 2020, **11**, 421–431.
61 N. M. Vargas-Barbosa and B. Roling, *ChemElectroChem*, 2020, **7**, 367–385.
62 A. Gheribi, K. Machado, D. Zanghi, C. Bessada, M. Salanne and P. P. Chartrand, *Electrochim. Acta*, 2018, **274**, 266–273.
63 H. Fanf and P. Jena, *Nat. Commun.*, 2022, **13**, 2078.
64 D. Frenkel and B. Smit, *Understanding Molecular Simulation, from Algorithms to Applications, Computational Science, from Theory to Applications (Academic)*, 2001.
65 M. Allen and D. J. Tildesley, *Computer Simulation of Liquids*, Oxford University Press, USA, 1989.
66 A. V. der Ven, G. Ceder, M. Asta and P. Tepesch, *Phys. Rev. B: Condens. Matter Mater. Phys.*, 2001, **64**, 184307.
67 L. Haarmann and K. Albe, *Solid State Ionics*, 2021, **363**, 115604.
68 S. Sicolo, C. Kalcher, S. Sedlmaier, J. Janek and K. Albe, *Solid State Ionics*, 2018, **319**, 83–91.
69 Y. Gao, A. Nolan, P. Du, Y. Wun, C. Yang, Q. Chen, Y. Mo and S. Bo, *Chem. Rev.*, 2020, **120**, 5954–6008.
70 G. Murch, *Solid State Ionics*, 1982, **7**, 177–198.
71 W. Richards, T. Tsujimura, L. Miara, Y. Wang, J. Kim, S. Ong, I. Uechi, N. Suzuki and G. Ceder, *Nat. Commun.*, 2016, **7**, 1–8.
72 Z. Zhu, I. Chu, Z. Deng and S. Ong, *Chem. Mater.*, 2015, **27**, 8318–8325.
73 Y. Lin, A. Yong, W. Gustafson, C. Reedy, E. Ertekin, J. Krogstad and N. Perry, *Curr. Opin. Solid State Mater. Sci.*, 2020, **24**, 100875.
74 A. Marcolongo and N. Marzari, *Phys. Rev. Mater.*, 2017, **1**, 025402.
75 N. Molinari, Y. Xie, I. Leifer, A. Marcolongo, M. Kornblutha and B. Kozinsky, *Phys. Rev. Lett.*, 2021, **217**, 025901.
76 M. Mottet, A. Marcolongo, T. Laino and I. Tavernelli, *Phys. Rev. Mater.*, 2019, **3**, 035403.
77 P. Salmon and A. Zeidler, *J. Condens. Matter Phys.*, 2015, **27**, 133201.
78 A. Zeidler, P. Salmon, T. Usuki, S. Kohara, H. Fischer and M. Wilson, *J. Chem. Phys.*, 2022, **157**, 094504.
79 T. Pham, A. Samad, H. Kim and Y. Shin, *J. Appl. Phys.*, 2018, **124**, 164106.
80 D. Marx, *ChemPhysChem*, 2006, **7**, 1848–1870.
81 M. Tuckerman, D. Marx and M. Parrinello, *Nature*, 2002, **417**, 925–929.
82 M. Boero, T. Ikeshoji and K. Terakura, *ChemPhysChem*, 2005, **6**, 1775–1779.
83 K. Kamiya, M. Boero, M. Tateno, K. Shiraishi and A. Oshiyama, *J. Am. Chem. Soc.*, 2007, **129**, 9663–9673.
84 H. Ali, F. Giberti, J. Cuny, T. D. Kühne and M. Parrinello, *Proc. Natl. Acad. Sci. U.S.A.*, 2013, **110**, 13723–13728.
85 M. Hellstrom, M. Ceriotti and J. Behler, *J. Phys. Chem. B*, 2018, **122**, 10158–10171.
86 A. P. Bartók, R. A. Kondor and G. Csányi, *Phys. Rev. B: Condens. Matter Mater. Phys.*, 2013, **87**, 184115.
87 Z. El-Machachi, M. Wilson and V. L. Deringer, *Chem. Sci.*, 2022, **13**, 13720–13731.

88 N. Bernstein, B. Bhattarai, G. Csányi, D. A. Drabold, S. R. Elliott and V. L. Deringer, *Angew. Chem.*, 2019, **131**, 7131–7135.
89 L. Sun, Y.-X. Zhou, X.-D. Wang, Y.-H. Chen, V. L. Deringer, R. Mazzarello and W. Zhang, *npj Comput. Mater.*, 2021, **7**, 29.
90 Z. Lu, C. Chen, Z. M. Baiyee, X. Chen, C. Niu and F. Ciucci, *Phys. Chem. Chem. Phys.*, 2015, **17**, 32547–32555.
91 X. L. J. Howard, A. Chen, J. Zhu, S. Li, G. Wu, P. Dowden, H. Xu, Y. Zhao and Q. Jia, *Adv. Sci.*, 2016, **3**, 1500359.
92 J. Serejo, J. Pereira, R. Mouta and L. Rego, *Phys. Chem. Chem. Phys.*, 2021, **23**, 6964–6973.
93 A. Song, Y. Xiao, K. Turcheniuk, P. Upadhya, A. Ramanujapuram, J. Benson, A. Magasinski, M. Olguin, L. Meda, O. Borodin and G. Yushin, *Adv. Energy Mater.*, 2018, **8**, 1700971.
94 J. Howard, Z. Hood and N. Holzwarth, *Phys. Rev. Mater.*, 2017, **1**, 075406.
95 P.-C. Tsai, S. Mair, J. Smith, D. M. Halat, P.-H. Chien, K. Kim, D. Zhang, Y. Li, L. Yin, J. Liu, S. H. Lapidus, J. A. Reimer, N. P. Balsara, D. J. Siegel and Y.-M. Chiang, *Adv. Energy Mater.*, 2023, **13**, 2203284.
96 H. Fang and P. Jena, *Nat. Commun.*, 2022, **13**, 2078.
97 F. Fu, X. Chen, N. Yao, X. Shen, X. Ma, S. Feng, S. Wang, R. Zhang, L. Zhang and Q. Zhang, *J. Energy Chem.*, 2022, **70**, 59–66.
98 Z. Zhang and L. Nazar, *Nat. Rev. Mater.*, 2022, **7**, 389–405.
99 *Molecular Dynamics of Nanostructures and Nanoionics, Simulations in Complex Systems*, ed. J. Habasaki, eBook, Imprint Jenny Stanford Publishing, New York, 2020.
100 F. Wang, H. A. Evans, K. Kim, L. Yin, Y. Li, P.-C. Tsai, J. Liu, S. H. Lapidus, C. M. Brown, D. J. Siegel and Y.-M. Chiang, *Chem. Mater.*, 2020, **32**, 8481–8491.
101 *Data Deposited and Available at NOMAD*, **https://doi.org/10.17172/NOMAD/2023.03.06-1**.